Burns & Trauma, 2026, **14**, tkaf072
https://doi.org/10.1093/burnst/tkaf072
Published: 14 November 2025
Research Article

OXFORD

Sequential treatment of infectious bone defects with three dimensional-printed body temperature-responsive shape memory scaffold coated with metal-polyphenol layers

Shuhao Yang[1,‡], Qianshui Hu[1,‡], Yingkun Hu[1,‡], Zhengguang Pu[2], Yixuan Lan[2], Haoming Wu[2], Gaohui Zhu[3], Zhixiang Gao[1], Jianye Yang[1], Shuai Tan[3], Ning Hu[1,*], Xulin Hu[2,4,*], Leilei Qin[1,*]

[1]Department of Orthopaedic Surgery, Chongqing Municipal Health Commission Key Laboratory of Musculoskeletal Regeneration and Translational Medicine/Orthopaedic Research Laboratory, The First Affiliated Hospital of Chongqing Medical University, No. 1 Youyi Road, Yuanjiagang, Yuzhong District, Chongqing 400042, China
[2]Clinical Medical College and Affiliated Hospital of Chengdu University, Chengdu University, No. 82, North Section 2, 2nd Ring Road, Chengdu, Sichuan 610106, China
[3]Department of Endocrinology Children's Hospital of Chongqing Medical University, National Clinical Research Center for Child Health and Disorders, Ministry of Education Key Laboratory of Child Development and Disorders, China International Science and Technology Cooperation base of Child Development and Critical Disorders, Chongqing Key Laboratory of Child Rare Diseases in Infection and Immunity, No. 136, Zhongshan 2nd Road, Yuzhong District, Chongqing 400014, China
[4]Department of Biotherapy, Cancer Center and State Key Laboratory of Biotherapy, West China Hospital, Sichuan University, No. 17, Section 3, Renmin South Road, Wuhou District, Chengdu, Sichuan 610041, China

*Corresponding authors. Xulin Hu, Clinical Medical College and Affiliated Hospital of Chengdu University, Chengdu University, No. 19, Section 3, Renmin South Road, Wuhou District, Chengdu, Sichuan 610106, China, E-mail: huxulin1993@163.com; Leilei Qin, The First Affiliated Hospital of Chongqing Medical University, Chongqing Medical University, No. 1, Youyi Road, Yuzhong District, Chongqing 400042, China, E-mail: 253505921@qq.com; Ning Hu, The First Affiliated Hospital of Chongqing Medical University, Chongqing Medical University, No. 1, Youyi Road, Yuzhong District, Chongqing 400042, China, E-mail: huncqjoint@yeah.net
‡Shuhao Yang, Qianshui Hu, and Yingkun Hu contributed equally to this work.

Abstract

Background: **Infectious bone defects are characterized by persistent bacterial invasion and an immune microenvironment imbalance, which significantly hinders bone regeneration. Recently, numerous bone repair materials have been developed to address the complex pathological microenvironment associated with infectious bone defects. However, dynamic changes in the defect size after infectious debridement pose a significant challenge for achieving effective bone integration of artificial bone grafts. Therefore, there is a need to develop an integrated scaffold with antibacterial, immunomodulatory, and osteogenic properties to achieve filling of irregular bone defects.**

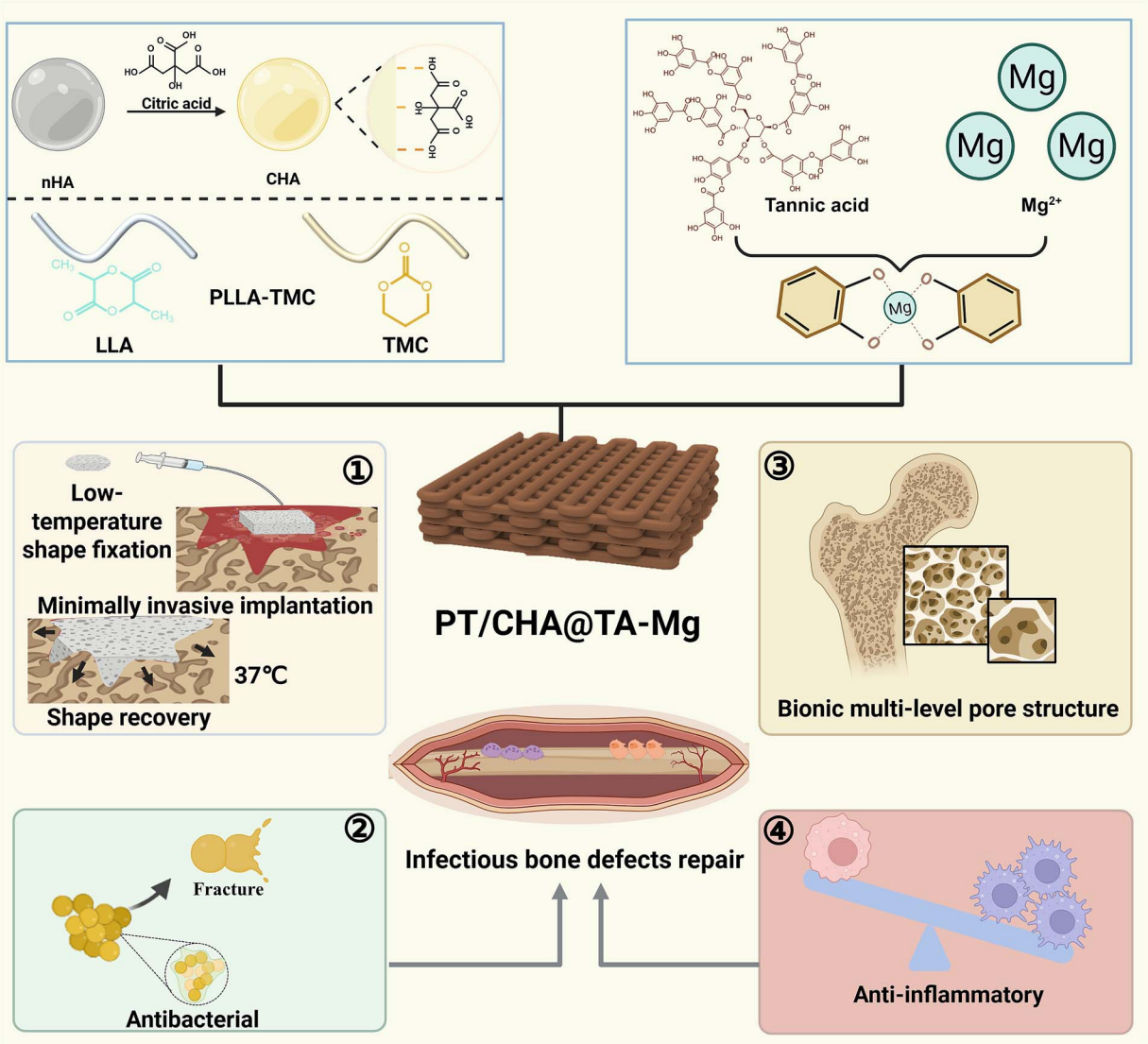
Methods: **Using low-temperature printing combined with the freeze-drying technology, a shape-memory scaffold with a biomimetic porous structure of cancellous bones was fabricated by compositing left-handed poly(L-lactic acid)-trimethylene carbonate (PLLA-TMC) with citric acid-modified hydroxyapatite (CHA). The scaffold (PT/CHA) was further coated with a metal-polyphenol network tannic acid-magnesium (TA-Mg) on its surface through the "mussel" effect, enabling the sequential treatment of infectious bone defects.**

Results: **The scaffold can adaptively integrate with defect interfaces at the physiological temperature (37°C), achieving superior bone integration performance. The incorporation of citric-acid-modified hydroxyapatite effectively optimizes the polymer-inorganic phase printing ink system, significantly enhancing the mechanical strength and mineralization capacity of the scaffold. Meanwhile, the external tannic-acid-magnesium metal-polyphenol coating (TA-Mg) demonstrates excellent pathogen clearance properties both *in vitro* and *in vivo*. It also influences macrophage polarization to regulate the immune microenvironment, ultimately promoting bone regeneration in infectious bone defects.**

Conclusions: **The PT/CHA@TA-Mg scaffold achieves bone integration through adaptive filling and enables the multi-stage treatment of infectious bone defects via antibacterial, immune-regulatory, and osteogenic differentiation.**

Received: 9 July 2025. **Revised:** 2 November 2025. **Accepted:** 5 November 2025
© The Author(s) 2025. Published by Oxford University Press.
This is an Open Access article distributed under the terms of the Creative Commons Attribution-NonCommercial License (https://creativecommons.org/licenses/by-nc/4.0/), which permits non-commercial re-use, distribution, and reproduction in any medium, provided the original work is properly cited. For commercial re-use, please contact reprints@oup.com for reprints and translation rights for reprints. All other permissions can be obtained through our RightsLink service via the Permissions link on the article page on our site—for further information please contact journals.permissions@oup.com.

Downloaded from academic.oup.com/burnstrauma/article/doi/10.1093/burnst/tkaf072/8317955 by guest on 12 October 2026



Keywords Infectious bone defect, Low-temperature 3D printing, Shape memory, Osseointegration, Antibacterial, Anti-inflamation, Scaffolds

Highlights

- **Shape memory scaffold adaptive filling of irregular bone defects.**
- **Optimization of low-temperature printing system by modifying hydroxyapatite.**
- **The multi-level pore structure of biomimetic cancellous bone.**
- **Metal-polyphenol coating for Infection control and osteoinduction.**

Background

Infected bone defects (IBDs) refer to the progressive destruction and defects in bone tissues caused by pathogenic microorganisms, such as *Staphylococcus aureus* (*S. aureus*) and *Escherichia coli* (*E. coli*). IBDs are commonly observed in osteomyelitis, post-traumatic chronic bone infections, and other pathological processes [1]. These defects not only lead to structural instability and dysfunctions of bones, but may also lead to long-term infections, which, in severe cases, require surgical repair or reconstruction [2]. Unlike conventional bone defects, the treatment of IBDs not only requires implants to ensure good bone performance, but also needs to achieve effective inhibition of the infected microenvironment [3]. Currently, high-dose vancomycin rinses and intravenous injections are mainly used to control early infections. Still, an increase in the proportion of drug-resistant bacteria and the cytotoxicity of high-concentration antibiotics to surrounding tissues limit their clinical application [4]. In addition, imbalance in the immune polarization of macrophages in the early stage of bone infections is one of the key factors inhibiting bone repair, which is usually due to the activation of M1-type polarization of macrophages via pathogens through their virulence factors (e.g. α-hemolysin), promoting the secretion of pro-inflammatory factors (e.g. TNF-α, IL-1β, and IL-6) to aggravate local inflammatory

Downloaded from academic.oup.com/burnstrauma/article/doi/10.1093/burnst/tkaf072/8317955 by guest on 12 October 2026

reactions and thereby suppressing the osteogenesis of mesenchymal stem cell (BMSC) osteogenic differentiation [5–7]. In conclusion, the effective removal of pathogenic bacteria within an infected microenvironment while suppressing the excessive inflammatory response is particularly important for the repair of IBDs.

Currently, various types of artificial bone scaffolds (hydrogels, ceramics, and metals) have been used to regulate the immune microenvironment of bone defects by loading bioactive small molecules [8]. Among them, hydrogels can realize controlled drug release due to their excellent ECM-like structure network and good injectability [9], but their inherent low mechanical strength cannot provide mechanical support at the filling sites [10]. Ceramic-based scaffolds, which are highly similar to the composition of inorganic salts in bone tissues, have excellent osteoconductivity, but their intrinsic mechanical fragility also prevents them from realizing local stress support [11]. Although metal scaffolds have good mechanical support properties, they are subject to the "stress shielding" effect that often leads to localized osteolysis, and their rigid structure is unable to cope with the dynamics of defects caused by bone infections and debridement during the implantation process [12, 13]. In conclusion, existing implant systems fail to accurately achieve a mechanical and structural integration in the affected regions of bone defects. Therefore, in order for scaffolds to effectively exert their biological effects, they must possess a geometry matching the defect spaces and provide adequate mechanical support. In recent years, to achieve adaptive filling of complex bone defects, researchers have begun to focus on intelligent scaffolds that can dynamically adjust their structure.

Shape memory scaffolds (SMSs) demonstrate remarkable potential for dynamic structural modulation, enabled by their capacity to transition between initial and programmed shapes in response to external stimuli such as light, temperature, liquids, or electric fields [14, 15]. Biodegradable temperature-responsive materials, exemplified by polylactic acid (PLA), exhibit shape-changing properties around the glass transition temperature (Tg). This characteristic significantly improves their ability to conform to irregular defects [16]. However, the intrinsic acidic degradation characteristic of PLA may exacerbate local tissue inflammation, leading to osteoclast activation and impaired osteoblast differentiation [17]. In our previous studies, we developed a shape memory polymer system, PLLA-TMC (PT), that integrates control over shape memory recovery performance, mechanical strength and degradation behavior, which was achieved by copolymerizing poly(trimethyl carbonate) (PTMC), exhibiting neutral degradation characteristics, with poly(L-lactic acid) (PLLA) at various ratios (8:2, 7:3, and 6:4). Additionally, the Tg of the material was tuned to approach human body temperature (37°C), enabling it to achieve self-adaptive filling upon implantation and thereby enhancing its integration efficiency [18, 19]. However, due to the inherent limitations of polymers, the scaffolds constructed from such copolymers still suffer from insufficient mechanical strength and surface biological inertness, hindering the effective transition of mechanical and biological signals. Blending with an inorganic phase is an effective approach to enhance their mechanical properties. Nevertheless, conventional high-temperature molding methods fail to achieve an efficient incorporation of the inorganic phase and cause polymer degradation during processing, thereby compromising mechanical integrity. Low-temperature 3D printing technology enables the incorporation of bioactive molecules into printing inks while avoiding the thermal degradation of materials. Moreover, this technique facilitates the construction of a macroscopic macroporous network structure along with secondary pore structures that promote stem cell proliferation and differentiation, achieving the macro–micro biomimicry of bone tissue architectures [20].

As a commonly-used inorganic reinforcement phase in printing systems, nanohydroxyapatite (nHA), as the main component of bone inorganic salts, has shown outstanding performance in improving the mechanical strength of scaffolds. However, its poor osteoinductive and cell adhesion properties still fail to improve the efficiency of bone repair [21]. In addition, its large surface energy and hydrophilicity tend to aggregate through van der Waals forces, hydrogen bonds and other forces, which impede its dispersion in solutions and make it difficult to maximize encapsulation in printing inks [22]. For this reason, various methods have been developed to enhance the bioactivity of nHA and improve its surface energy. Citric acid (2-hydroxy-1,2,3-propanetricarboxylic acid), as a natural weak organic acid, has been widely used in the preparation of novel biodegradable biomaterials for its ability to regulate cellular metabolism and stem cell differentiation through energy metabolism, vascular growth as well as immunomodulation [23]. Meanwhile, the carboxyl group (-COOH) and other groups in its molecule can change the surface charge of nano-hydroxyapatite by respectively coordinating with calcium or hydroxide ions on its surface, to weaken the electrostatic attraction or repulsion among particles [24]. In addition, citric acid can promote inorganic salt matrix calcium-phosphorus deposition to enhance mineralization by decreasing free Ca^{2+} concentration and crystal-specific adsorption [25]. Therefore, modification through citric acid is expected to improve the agglomeration behavior of nHA in polymer print ink systems while increasing the mineralization level of scaffolds.

To address the complex inflammatory microenvironment and diverse pathogenic bacteria in bone infections, numerous bioactive molecules have been extensively employed. However, achieving an effective synergistic antibacterial and anti-inflammatory effect remains challenging. Natural polyphenols, exemplified by tannic acid (TA), exhibit remarkable antibacterial and anti-inflammatory properties owing to their abundant aromatic rings and hydroxyl groups [26]. At the same time, their "mussel-like" effect can be stabilized through non-covalent bonding and adsorbed on the surface of materials, improving the hydrophobicity of inert polymeric material surfaces [27]. However, highly active phenolic hydroxyl groups are often prone to be inactivated too quickly by pH and temperature, etc., thus reducing their biological activity. Based on the highly abundant phenolic hydroxyl groups in polyphenolic drugs, metal phenolic networks (MPNs) can be constructed by forming coordination bonds with metal ions (Zn, Mg, and Cu, etc.). This stable composite structure protects the bioactivity of polyphenols and at the same time, exerts the bone-enhancing properties of metal ions under chelation [28]. Among many metal ions, Mg^{2+} shows less cytotoxicity and can stimulate osteoblast differentiation by activating Wnt/β-catenin and ERK signaling pathways, which shows great potential in the field of bone repair [29]. In addition, a self-assembled MPN network is able to achieve the rapid release of active substances in response to infected microacidic

Downloaded from academic.oup.com/burnstrauma/article/doi/10.1093/burnst/tkaf072/8317955 by guest on 12 October 2026

environments for timely interventions. Therefore, utilizing Mg^{2+} and TA to construct metal-polyphenol network coatings to modify bone-filled implants can effectively control the microenvironment at the early stage of infections.

In this study, we constructed a shape memory bionic scaffold (PT/CHA@TA-Mg) with integrated antibacterial–anti-inflammatory–osteogenic functions based on low-temperature 3D printing and coating assembly technologies. The citric acid-modified nHA (CHA) was used as an inorganic phase composite PLA-TMC to prepare the cryogenic printing ink; meanwhile, the good dispersion property of CHA in the polymer solution and the precise regulation of printing parameters were utilized to achieve the increase of inorganic salt encapsulation, which in turn improved the mechanical strength and mineralization level of the scaffold. In addition, the scaffolds constructed through the combination of low-temperature printing and freeze-drying technologies can quickly respond to the shape recovery of body temperature environments after filling to achieve the integration of irregular defect boundaries, and at the same time, its macropores, internal pores and surface topology micropores meet the multi-level pore structure of bionic cancellous bones, which is more conducive to the growth of bone tissues. Further, relying on the strong phenolic functional group of TA, it can effectively achieve adhesion on scaffold surfaces through non-covalent bonding and chelate Mg^{2+} to form a metal-polyphenol network for responsive release under acidic conditions to achieve effective antimicrobial behavior in the early stage of infections, as well as the modulation of the immune microenvironment. In conclusion, this anti-infective enabling bone cascade bone repair scaffold provides a new therapeutic option for the treatment of IBDs (Figure 1).

Methods

Materials

PLLA-TMC (mass ratio 70:30, Mw = 225 kDa; hereinafter referred to as PT) was synthesized in our laboratory with reference to previous work [30]. The purified PT chemical structure was analyzed by ^{1}H NMR (400 MHz, Avance III, Germany) (Figure S1). nHA (particle size: 60 ∼ 80 nm, CAS: 1306-06-5), citric acid (CAS: 77–92-9), TA (CAS: 1401-55-4), dopamine hydrochloride (purity ≥95%; CAS: 62–31-7) and magnesium chloride (CAS: 7786-30-3) were purchased from Maclean's Chemical Company Limited, China. All other reagents and organic solvents used for cell culture and other experiments were of ACS grade and could be used directly without further purification.

Preparation and characterization of citric acid-modified hydroxyapatite

Nano hydroxyapatite was added to deionized water and sonicated for 1.5 h to obtain a well-dispersed suspension of 0.01 g/ml. Subsequently, 0.001 g/ml citric acid solution was configured and the pH was adjusted to 7–8. The configured citric acid solution was dropped into the nHA suspension and stirred at 37°C for 6 h. After stirring, the reaction was stopped by centrifugation and washed with anhydrous ethanol several times, and CHA powder was obtained by freeze-drying.

The micromorphology of CHA was analyzed by transmission electron microscopy (TEM, JEOL, Japan) with an accelerating voltage of 120 kV. The crystalline phase of CHA powder was detected using an X-ray diffractometer (XRD, Rayto Life and Analytical Sciences, China). The characteristic peak variations of CHA powders were observed using an FTIR spectrometer (Cary 630 FTIR spectrometer, Agilent Technologies, USA) in the range of 4000–500 cm^{-1} wave number in total reflection mode. The dispersibility was observed by dispersing 1 g of nHA or CHA powder in a 1:20 (w/v) ratio in a dioxane solution and leaving it for 30 min. The 3D printing ink extrusion performance was verified by a dynamic rheometer (AR 2000 ex, TA Instruments, USA). Specifically, an 8 mm parallel plate was used for the experiment, with a 1 mm gap between the upper and lower plates to ensure uniform stress application. The test environment temperature was maintained at 25°C. For frequency sweep analysis, the ink was subjected to angular frequency scanning under a stress of 100 Pa. For viscosity testing, we measured the shear stress/viscosity as a function of shear rate at rotational shear rates ranging from 0.01 to 100 s^{-1}. For the dynamic oscillatory strain experiment, we applied 1% and 100% oscillatory strain at the corresponding time points under a constant frequency of 1 Hz to observe the changes in the ink modulus.

Fabrication of three dimensional-printing PT/CHA@TA-Mg scaffolds

A multifunctional 3D printer (EFL-BP-6601, Yongqinquan Intelligent Equipment Co., Ltd, Suzhou, China) was utilized for the programming of printing parameters and the preparation of porous scaffolds. The scaffolds were constructed using a low-temperature printing platform, with the temperature of the printing ice plate at −5°C, the temperature of the printing nozzle at 25°C, the diameter of the printing needle at 21G, 0.8 mm, the height of the first layer at 0.35 mm, and the speed of the printing at 40 mm/s. The scaffolds were pre-frozen for 12 h in a refrigerator at −20°C and then freeze-dried for 2 days. The scaffolds were then dried in an oven at 37°C for 3 days to remove residual organic solvents. To prepare the TA-Mg coating, 1.00 g of TA was first dissolved in 50 ml of deionized water. The pH of the solution was then adjusted to 7.4 by dropwise addition of 0.1 M NaOH. Subsequently, 0.20 g of magnesium chloride was slowly added to the solution under rapid stirring. The mixture was then subjected to ultrasonic dispersion for 5 min. Next, the PT/CHA scaffold was immersed in the solution and reacted at 25°C for 4 h. After the reaction, the scaffold was rinsed three times with deionized water and dried at 50°C for 6 h. This process was repeated five times to achieve gradient deposition, ultimately yielding the PT/CHA@TA-Mg scaffold. In the subsequent part of the article, the scaffolds printed with PT alone were named PT; the scaffolds co-mixed with PT and CHA in the printing ink were named PT/CHA; the scaffolds modified with TA coating on the PT/CHA surface were named PT/CHA@TA; and the scaffolds modified with TA-Mg coating on the PT/CHA surface were named PT/CHA@TA-Mg.

Downloaded from academic.oup.com/burnstrauma/article/doi/10.1093/burnst/tkaf072/8317955 by guest on 12 October 2026

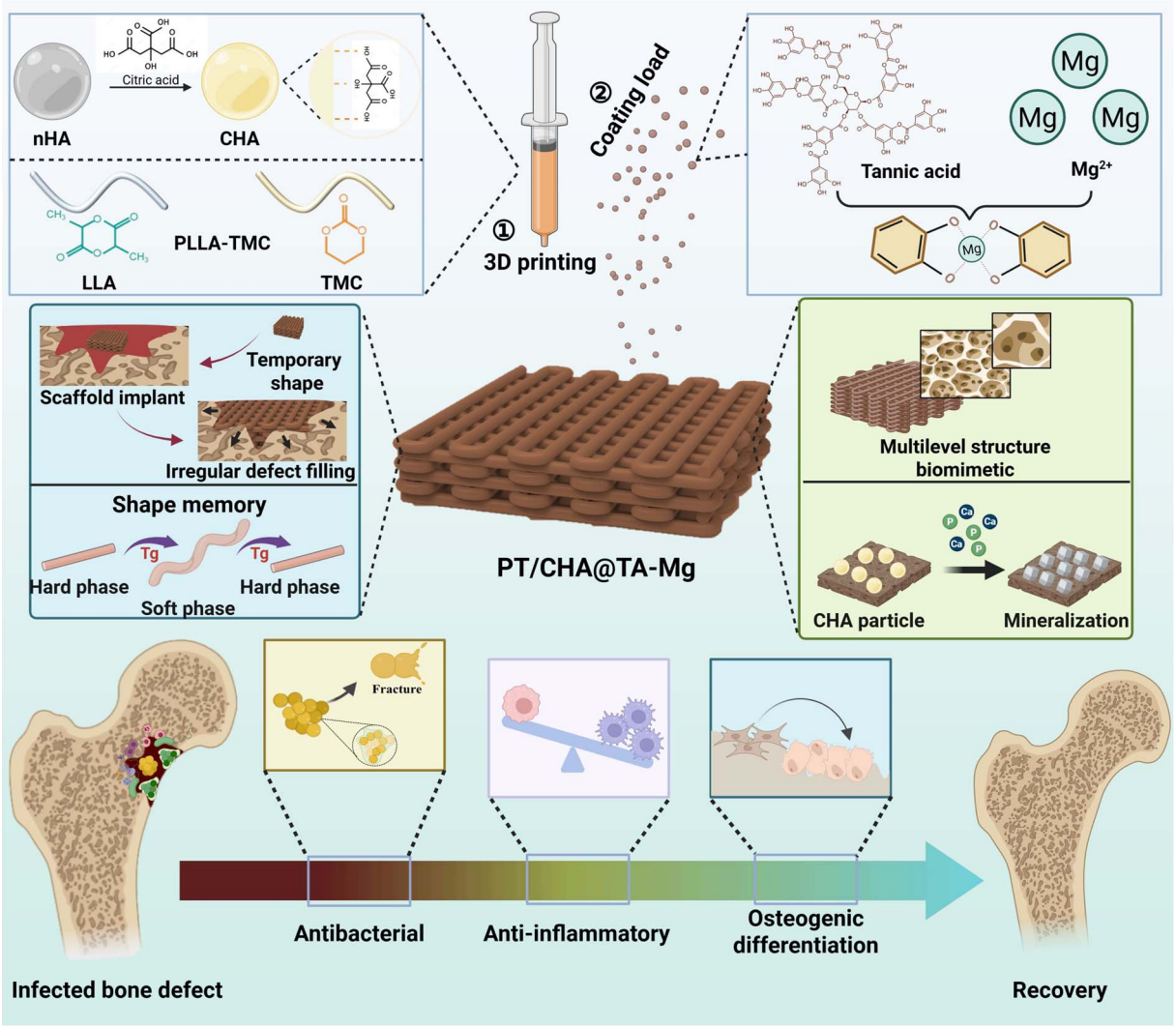


Figure 1 3D printed SMSs with bionic multilevel structures synergistically treat infected bone defects by loading TA-Mg metal-polyphenol coatings. *CHA* citric acid-modified hydroxyapatite, *LLA* L-lactic acid, *TMC* trimethylene carbonate

Structural and morphological characterization of three dimensional-printing PT/CHA@TA-Mg scaffolds

The surface and cross-sectional morphology of the scaffolds were observed using a scanning electron microscope (SEM, Quanta 250, USA) and tested for surface elemental distribution of the scaffolds using Energy Dispersive Spectroscopy (EDS) to test the elemental distribution on the surface of the scaffolds, and FTIR spectroscopy to observe the distribution of the characteristic peaks of PT, PT/CHA and PT/CHA@TA-Mg scaffolds. Further testing of the chemical composition of the coated scaffolds by X-ray photoelectron spectroscopy (XPS, XSAM 600, U.K.) was further employed. The surface roughness of the scaffolds was determined using scanning probe microscopy (SPM; Cypher VRS, Oxford, UK). The hydrophilicity of the scaffold surface was measured by a water contact angle meter (JY-82 B, Chengde Dingsheng, China). Differential scanning calorimetry (DSC) was used to analyze PT and PT/CHA. Specifically, the samples were heated from 0°C to 150°C at a rate of 10°C/min, then cooled at the same rate to 0°C, and finally heated again to 150°C. During the second heating process, the glass transition temperature of the samples was measured. The compression performance of the scaffold was tested using a universal mechanical testing machine, specifically preparing a scaffold with specifications of 10 mm × 10 mm × 3 mm, using a stress load of 20 kN and compression testing at a loading rate of 0.5 mm/min, and compression modulus calculations using the national standard GB 7314–87. The Archimedes method is adopted to measure the porosity of the scaffold. In simple terms, the porosity is calculated by the ratio of the volume of the pores filled with ethanol to the total volume of the scaffold. Firstly, the pores of the scaffold are filled with liquid. By measuring the volume of the liquid and the volume of the scaffold, the porosity of the scaffold can be obtained.

The equation for calculating the water absorption of the scaffold is as follows:

$$\text{Water absorption } (\%) = (W2 - W1)\,/W1 \times 100 \quad (1)$$

Downloaded from academic.oup.com/burnstrauma/article/doi/10.1093/burnst/tkaf072/8317955 by guest on 12 October 2026

Where W2 is the mass of the scaffold after water absorption and W1 is the dry weight of the scaffold before water absorption.

In vitro 2,2-diphenyl-1-picrylhydrazyl radical scavenging

The antioxidant capacity of the scaffolds was evaluated using the 2,2-diphenyl-1-picrylhydrazyl (DPPH) free radical kit. Specifically, the scaffold samples were added to 3 ml of DPPH ethanol solution and DPPH solution alone was used as a blank group. After the reaction was carried out for 30 min at room temperature and protected from light, the absorbance value of the reaction system was measured at 515 nm using a UV spectrophotometer. The antioxidant capacity of the scaffolds was assessed by calculating the DPPH radical scavenging rate by determining the absorbance values of the sample group versus the blank control group (DPPH solution without sample). The DPPH scavenging rate was calculated by the following equation:

$$\text{DPPH scavenging}\ (\%) = (\text{Ablank} - \text{Ascaffolds})/\text{Ablank}) \times 100 \quad (2)$$

Where Ablank is the absorbance of the blank solution and Ascaffolds is the absorbance of the solution after the addition of the scaffold.

Scaffold degradation experiment

Scaffolds were subjected to enzymatic degradation in phosphate-buffered saline (PBS, pH 7.4) containing lipase at a final concentration of 1 mg/ml and incubated at 37°C. Samples were collected at 2, 4, 6, and 8 weeks, weighed to calculate mass loss, and the pH of the degradation medium was measured. After weighing, the samples were further examined by SEM.

Drug release determination

The composite scaffolds were placed in phosphate buffer at pH 5.5 and pH 7.4 at a ratio of 1:20 (w/v), respectively, and placed in a constant temperature shaker (100 rpm) at 37°C for *in vitro* release experiments. Samples were taken at regular intervals (3, 6, 9, 12, 15, and 18 days), and an equal volume of fresh PBS was replenished immediately after each sample to maintain the funnel conditions. After centrifugation (12 000 rpm, 5 min) of the removed sample solution, the absorbance value of the supernatant was determined by a UV spectrophotometer and the cumulative drug release was calculated based on the standard curve of TA. The release of magnesium ions at different time intervals was quantified using inductively coupled plasma mass spectrometry (ICP-MS).

Shape memory function test

The shape-memory recovery of the fixed-shape scaffold was evaluated at 37°C. Scaffolds measuring 2 cm × 1 cm and 1 cm × 1 cm were first taken from a dry state and heated to 43°C for 1 min to curl into a temporary shape. The temporary shape was then fixed at a simulated surgical temperature of 20°C for 1 min. Finally, the scaffolds were returned to a simulated human body temperature of 37°C, and their shape-memory recovery was observed and recorded.

Extracellular mineralization behavior

The *in vitro* mineralization properties of the scaffolds were examined using SBF-simulated body fluids, specifically ∼0.5 g of the scaffolds (PT, PT/HA, and PT/CHA) were placed in SBF solution at a ratio of 1:20 (w/v) and incubated at 37°C for 7 days and the fluid was changed every 2 days, and the scaffolds were taken out after 7 days and the scaffolds were rinsed with deionized water for three times on the scaffold surfaces, and then dried at 37°C for 12 h for SEM observation. In addition, XRD was used to detect the crystalline phase of different scaffolds after mineralization.

In vitro biocompatibility evaluation

Rat femur-derived mesenchymal stem cells (BMSCs) were used for *in vitro* biocompatibility assessment of the scaffolds. The scaffolds were first sterilized under ultraviolet light for 24 h. The different groups of scaffolds were co-cultured with cells (1×10^4cells/well) in 24-well plates with modified medium (DMEM, Sigma-Aldrich) supplemented with 1% (v/v) penicillin and streptococcal tobramycin and 10% (s/v) fetal bovine serum (FBS) for 1 day and 3 days at 37°C in a 5% CO_2 environment. An acridine orange staining kit (Sigma-Aldrich) was used to evaluate the proliferation of BMSCs cells and to observe the cell proliferation on the well plates and scaffolds under an inverted fluorescence microscope (IX83, Olympus, Japan). Cell proliferation and differentiation were assessed using the CCK-8 cell counting kit (CK 04, Dojindo, Japan). Briefly, the sterilized scaffolds were soaked for 3 days and the extracts were extracted and co-cultured with cell suspension (100 μl per well) in 96-well plates for 1, 3, and 5 days, respectively, followed by the addition of 10 μl of CCK-8 reagent and the measurement of absorbance at 450 nm using an enzyme labeler (Varioskan LUX, Thermo, USA). TRITC-labeled ghost pen cyclic peptide and DAPI staining were used to observe the cytoskeleton of BMSCs. To capture the adhesion behavior of BMSCs on the scaffolds, the scaffolds from different groups were co-cultured with BMSCs for 3 days and then rinsed with PBS three times. Subsequently, they were fixed with 2.5% glutaraldehyde overnight and dehydrated through an ethanol gradient (70%, 75%, 80%, 85%, 90%, 95%, 100%) before SEM observation.

In vitro hemolysis test

Hemolytic activity was used to determine the blood compatibility of different groups. Specifically, 500 μl of rat blood was taken and centrifuged at 3500 rpm for 5 min at 4°C. The supernatant was removed and repeated three times. After resuspension with 5 ml of PBS, 1.5 ml of erythrocyte solution was placed in a centrifuge tube and samples of different groups were placed in it, followed by storing it at room temperature for 4 h. The samples were then removed from the tubes and centrifuged at 2000 rpm for 15 min and photographed for observation. The supernatant was removed and the absorbance at 545 nm was measured with an enzyme marker to calculate the hemolysis efficiency.

Downloaded from academic.oup.com/burnstrauma/article/doi/10.1093/burnst/tkaf072/8317955 by guest on 12 October 2026

Evaluation of osteogenic properties *in vitro*

The bone-enhancing function of the scaffolds was determined by measuring the degree of alkaline phosphatase (ALP) activity and expression. Specifically, scaffold extracts were co-cultured with 2×10^4 cells in 24-well plates for 2 days. Subsequently, the medium was changed to osteogenic induction medium with 10 μg ml-1 ascorbic acid and 10 mm β-glycerophosphate and every 2 days until the time point of analysis. After 7 and 14 days of incubation, respectively, ALP activity was determined using an ALP assay kit (Beyotime, China) and recorded by measuring absorbance at 405 nm using an enzyme marker. Referring to this culture method, the well plates were stained with CIP/NBT ALP Chromogenic Kit (Roche, Switzerland) on the 7 day to observe ALP deposition. For alizarin red staining (ARS), cells were fixed for 10 min after 3 rinses with PBS after 21 days of co-culture. Subsequently, alizarin red S staining solution (2%, pH 4.2, Beyotime, China) was applied to the samples and left at 37°C for 30 min before observation. Calcium deposition was measured by dissolving the stained calcium nodules in each well with 1 ml of 10% cetylpyridinium chloride (C129534, Aladdin, Shanghai), and the absorbance at 450 nm was measured after 30 min.

In vitro antibacterial assay

The inhibitory behavior of the coated scaffolds against *S. aureus* and *E. coli* was evaluated using a bacterial live-dead kit (Thermo Fisher, USA). Specifically, bacteria (1×10^6 CFU/ml) were incubated with the scaffolds at 37°C for 24 h and then the bacterial fluid was collected. After centrifugation, the centrifuge was resuspended in 2 ml of saline and an equal amount of mixed dye was added and incubated for 15 min away from light before being photographed under a fluorescence microscope. The plate counting method was also used to evaluate the antibacterial behavior of the scaffolds. Firstly, the scaffolds were incubated with bacteria in 5 ml of Tryptic Soy Broth (TSB, Sigma, USA) with shaking at 37°C for 12 h, and then diluted and placed on an agar plate and incubated for 24 h at 37°C and images were taken, and then colonies were counted and statistically counted by using ImageJ software. In addition, the scaffolds were co-cultured with the bacterial solution for 24 h and then rinsed with PBS three times before being fixed with 2.5 glutaraldehyde solution at 4°C for 2 h. After gradient dehydration of the scaffolds with 50%, 60%, 70%, 80%, 90%, and 100% ethanol solutions, respectively, the bacterial morphology on the scaffolds, as well as the destruction of bacterial membranes, was observed by scanning electron microscopy.

Macrophage polarization

RAW264.7 cells were inoculated in 24-well plates at a density of 1×10^5 using DMEM medium containing 10% FBS and 1% penicillin/streptomycin, and cultured to 80% fusion at 37°C in a 5% CO_2 incubator before being stimulated with 1 μg/ml lipopolysaccharide (LPS) for 24 h to induce polarization toward M1-type macrophages. Subsequently, the scaffold material was incubated at 37°C for 24 h and then centrifuged to obtain the extracts before co-culturing with RAW264.7 cells for 72 h, while a blank control group (containing DMEM medium only) and an LPS-positive control group were set up. At the end of the co-culture, the medium was aspirated, the cells were gently washed with pre-cooled PBS 3 times, fixed with 4% paraformaldehyde (PFA) for 10 min at room temperature, washed with PBS for 3 times, and then incubated with 5% bovine serum albumin (BSA) sealing solution for 1 h at room temperature to block the non-specific binding sites. Subsequently, the closed cells were incubated overnight with the following primary antibodies: CD86 (1:200, Abcam, USA) and CD206 (1:200, Proteintech, China), respectively, at 4°C. After washing three times with PBS, fluorescent-labeled secondary antibodies of the corresponding species (1:200, Abcam, USA) were added and incubated for 1 h at room temperature with protection from light, followed by cytoskeleton was stained with ghost pen cyclic peptide (1:200, Yeasen, China) for 30 min, and the nucleus was stained with DAPI (1:1000, Yeasen, China) for 10 min, and washed 3 times with PBS. Finally, fluorescence images were captured using an inverted fluorescence microscope and the fluorescence intensity was quantitatively analyzed by ImageJ. For flow cytometry analysis, RAW 264.7 cells were seeded in 24-well plates at a density of 1×10^5 cells/well. After the indicated treatments, cells were harvested and incubated with antibodies against CD86 (Biolegend, USA; 159 204) and CD206 (Biolegend, USA; 141 706) for 30 min at room temperature in the dark. Flow cytometric analysis was performed using a BD flow cytometer (BD Biosciences, USA). For Reverse Transcription Quantitative Polymerase Chain Reaction (RT-qPCR) analysis, total RNA was extracted using Trizol reagent (Beyotime, China), and reverse transcription was carried out with the HiScript III RT SuperMix kit (Vazyme, China). GAPDH was used as the internal control, and relative gene expression levels were calculated using the 2^-ΔΔCt method. Primer sequences are listed in Table S1 (Supporting Information).

Reactive oxygen species detection

RAW264.7 cells were seeded and then stimulated with 1 μg/ml LPS for 24 h. Subsequently, samples were added and co-treated for another 24 h. After treatment, cells were washed twice with PBS and incubated with 10 μm DCFH-DA probe in the culture medium for 30 min in the dark. The intracellular ROS levels were then detected using a flow cytometer (BD Biosciences, USA).

Infectious bone defect model

All *in vivo* ethical approvals were granted by the Animal Ethics Center of Sichuan University under the approval number YSY-DWLL-2023252. All rats were SD male rats weighing between 180–220 g. The rats were used for the study. After drilling a critical-size defect with a diameter of 5 mm and a depth of 3 mm in the lateral femoral condyle, 20 μl of *S. aureus* suspension with a concentration of 1×10^7 CFU ml^{-1} was injected into the defect and filled with scaffolds of different groupings and sutured to the muscle and the outer layer of skin layer by layer. Subsequent assessment of the degree of infection within the defect was performed at weeks 1 and 2, and neoplastic bone reconstruction was assessed by Micro-CT at week 8. On day 7 post-implantation, blood samples were collected from SD rats and allowed to clot at room temperature for 30 min. Serum was obtained by centrifugation at 1500 × g for 10 min at 4°C, after which the supernatant was carefully aliquoted. The concentrations of TNF-α and IL-10 were quantified using ELISA kits (Beyotime, China).

Downloaded from academic.oup.com/burnstrauma/article/doi/10.1093/burnst/tkaf072/8317955 by guest on 12 October 2026

Evaluation of *in vivo* antibacterial performance

Fourteen days after implantation, rats were euthanized and femoral samples were collected for gross view photography and cultured in Luria-Bertani medium for 12 h. 7 days after implantation of the scaffolds, tissues surrounding the implanted material were collected at the model establishment site and cultured in TSB and then counted for colonies on agar plates. In addition, hematoxylin and eosin (H&E) and Gram staining were performed on the collected tissue surrounding the material.

Microcomputed tomography assessment

Femoral heads were analyzed using microcomputed tomography (micro-CT) after fixation in 4% PFA solution for 48 h. The defect area was scanned using a micro-computed tomography scanner (45 μCT; SCANCO Medical, Switzerland) with a spatial resolution of 14.6 μm. Scanning parameters were set as follows: tube voltage 70 kV, tube current 114.0 μA, exposure time 240.0 ms, and voxel size 10 μm. Evaluation parameters included bone volume fraction (BV/TV), trabecular thickness (Tb.Th), trabecular number (Tb.N), and trabecular separation (Tb.Sp).

Histological assessment

After 8 weeks, the collected bone tissues were decalcified in 10% ethylenediaminetetraacetic acid (EDTA) solution for 1 month, processed for H&E staining and Masson trichrome staining after dehydration, paraffin embedding, and sectioning, respectively. Immunohistochemical staining of OCN was performed for observation. Semi-quantitative analysis of OCN positively stained cells was performed using ImageJ.

Statistical analysis

All data were collected from at least triplicated samples and expressed as the mean $\pm$ standard deviation (SD). All the quantitative data in each experiment were evaluated and analyzed using one-way ANOVA and Tukey's multiple comparisons test for multiple-group analysis in GraphPad Prism 9.2. A *P*-value of <0.05 was used as a statistical significance threshold. Statistical significance was considered at $^{*}P<0.05$, $^{**}P<0.01$, $^{***}P<0.001$, $^{****}P<0.0001$, "ns" presents $P>0.05$.

Results

Preparation and characterization of citric acid-modified hydroxyapatite

The content of inorganic salts in bone repair scaffold fabrication is constrained by the extrusion properties of printing inks, and nano-hydroxyapatite tends to aggregate in solvents due to its high surface energy, thereby affecting the extrusion performance of printing inks. To address this issue, citric acid was employed to modify hydroxyapatite, enhancing its dispersibility in polymer solutions (Figure 2a). The particle size distributions of nHA and CHA were separately characterized using TEM (Figure 2b). nHA showed obvious agglomeration behavior in an ethanol solution, whereas CHA modified with citric acid presented a uniform and dispersed short-rod shape, and it was also confirmed by SEM images that such modification made a better improvement on the dispersion of hydroxyapatite (Figure S2). To investigate the dispersive behavior of inorganic salt particles in printing inks before and after modification, nHA and CHA of the same mass were dispersed in a PT/dioxane solution at a ratio of 1:8 (w/v) respectively for 2, 4, and 6 h of static observation, and it was found that nHA was rapidly precipitated at the bottom of the bottle in a short period whereas CHA continued to be dispersed in the polymer solution, which further confirms that modified CHA has a good dispersive property and dispersibility, which can be added as an inorganic phase in printing inks (Figure 2c). The FTIR spectra analyzed changes in the characteristic peaks of nHA before and after modification (Figure 2d). The characteristic peaks at 560 cm^{-1} and 600 cm^{-1} were the Ca-O peak and P-O bending vibration peak of nHA, respectively, and the P-O stretching vibration peak from nHA was at 1050 cm^{-1}. In addition to the characteristic peaks of CHA, the C-O stretching vibration from citric acid, especially the resonance peak of carboxyl groups, was observed at 1400 cm^{-1}, and a new peak was also observed near 1650 cm^{-1}, which might be attributed to the C=O stretching vibration peak of the citric acid molecules, whose carboxyl groups interacted with the nHA surface to increase the intensity of this peak. In addition, after modification with citric acid, the O-H stretching vibration peak at 3400 cm^{-1} belonging to nHA was slightly changed, which could be attributed to the alteration of the hydroxyl groups of nHA through citric acid [31]. The crystalline peaks of nHA and CHA were separately characterized by XRD (Figure 2e). The XRD peaks of nHA corresponding to crystalline surfaces such as (211), (300), and (222) matched with the data cited in JCPDS N8 09-0432, whereas CHA appeared to have higher crystalline peaks at 25.8°, 31.7°, 32.7°, 39.6°, and 49.3°. The higher crystallinity of surface CHA might also be due to the complexation of citric acid with calcium ions and phosphates in nHA, thereby promoting the increased ordering of nHA structure.

To investigate the effect of citric acid on the modification of nHA on the extrusion performance of printing inks, CHA of different concentrations (10%, 20%, and 30%, w/w) and nHA printing inks were extruded (Figure 2f), and it could be observed that the addition of 30% of CHA could be easily extruded out of the nozzle, while 20% of nHA in the nozzle clogging, during the removal of the needle, could be observed in the white agglomerates, confirming the improved dispersion of nHA. The printhead temperature and the solvent ratio of printing inks would also have a significant impact on the molding condition of the scaffold, so we explored different solvent ratios (1:4, 1:5, and 1:6, w/v) at different printing temperatures under the printing condition (Figure 2g), finding it difficult to extrude the printing inks when the printing temperature was $\leq$10°C, and that printing inks of different ratios could have better molding properties at a printing temperature of 20°C. In addition, higher temperatures and solvent ratios increased the fluidity of inks, which reduced the moldability of the support, so a printing temperature of 20°C was chosen for subsequent printing. A rheological analysis was conducted using printing inks. In the frequency-modulus test (Figure 2h), the storage modulus (G′) of both PT and PT/30CHA printing inks was higher than the loss modulus (G″) at low angular frequencies (0.1–1 Hz), indicating that polymer long chains formed a solid-like network in the solvent, ensuring the stability of the inks'

Downloaded from academic.oup.com/burnstrauma/article/doi/10.1093/burnst/tkaf072/8317955 by guest on 12 October 2026

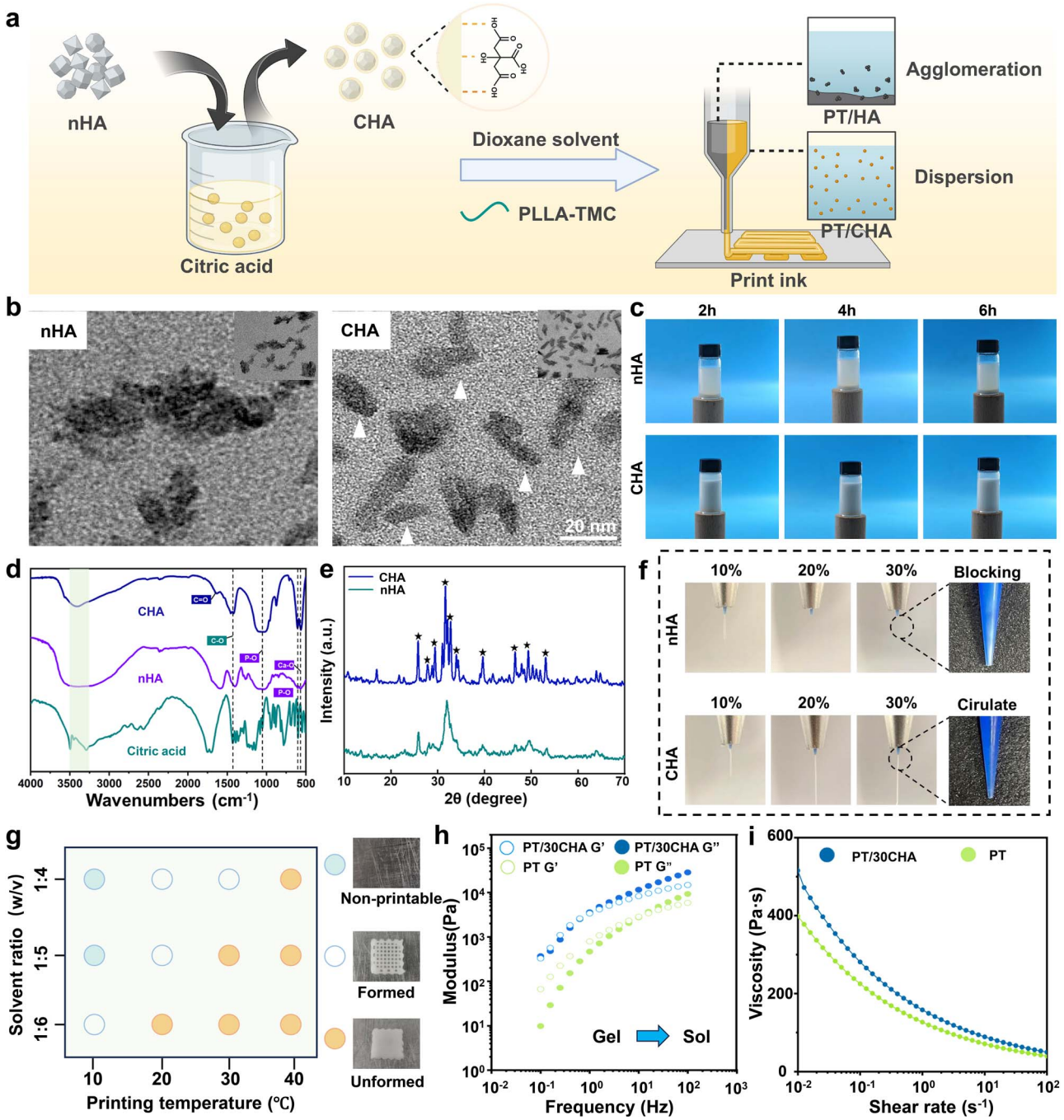


Figure 2 Characterization of citric acid-modified hydroxyapatite and its effect on printing ink. (**a**) Schematic representation of citric acid modified nano-hydroxyapatite agglomeration in solution. (**b**) TEM images of nHA and CHA. (**c**) Dispersion of nHA and CHA in polymer solution. (**d**) FTIR images of citric acid, nHA, and CHA. (**e**) XRD images of nHA and CHA. (**f**) Extrudability of nHA and CHA printing inks. (**g**) Effect of printing temperature and solvent ratio on printability. (**h**) Frequency scanning of printing inks. (**i**) Printing ink viscosity test. Data are expressed as mean ± SD. $^{*}P < 0.05$, $^{**}P < 0.01$, $^{***}P < 0.001$, $^{****}P < 0.0001$, $n = 3$. *nHA* nano hydroxyapatite, *CHA* citric acid-modified hydroxyapatite, *PT* poly(L-lactic acid)-trimethylene carbonate

extruded shape. This might be because the polymer molecular chains had more time to relax, stretch, and recover. At higher angular frequencies (>10 Hz), the loss modulus of the inks exhibited good fluidity, which increased with the increase of CHA content (Figure S3). This might be because at high frequencies, the molecular chain movement was shorter, and the inks exhibited energy dissipation behavior, thus showing a fluid state [32]. The extrusion performance of the inks was further evaluated through shear viscosity experiments (Figure 2i). The viscosities of both PT and PT/30CHA inks decreased with the increase of shear rate, and such shear thinning effect ensured controllable extrusion behavior of the inks [33]. Furthermore, to further verify the structure reconstruction ability of the inks during the extrusion process, we subjected them to dynamic oscillation strain experiments with 1% and 100% strain. The results showed that the modulus of the inks rapidly decreased under high-strain conditions, while it maintained a relatively high modulus under low-strain conditions, demonstrating their excellent extrusion performance (Figure S4).

Downloaded from academic.oup.com/burnstrauma/article/doi/10.1093/burnst/tkaf072/8317955 by guest on 12 October 2026

Construction and characterization of three dimensional printed PT/CHA@TA-Mg scaffolds

Based on the construction of PT/CHA bone repair scaffolds using low-temperature printing, a metal-polyphenol network structure was constructed by chelating magnesium ions with tannins and deposited on the scaffold surfaces through the action of tannin-like "mussels" (Figure 3a). Figure 3b shows the scaffolds obtained from different treatments, in which those coated with TA and TA-Mg show a more obvious dark brown and brownish gray color. SEM images reveal that all scaffolds exhibit a spongy bone-like through-pore structure (≈500 μm), with no significant difference in their porosity (Figure S5). Such a biomimetic pore structure not only facilitates efficient nutrient transport but also supports the vascularization process by providing an optimal microenvironment. The cross-sectional structure showed a network of microporous structures (5–20 μm) generated by the volatilization of a dioxane solvent, which could effectively ensure that the scaffolds could guide the remodeling of bone units during the bone regeneration stage [34]. Further analyses of the scaffold surface structure revealed that the PT scaffolds exhibited a smooth morphology, while the PT/CHA scaffolds displayed a microporous structure (2–8 μm) due to the uniform distribution of CHA. In contrast, the PT/HA scaffolds fabricated through cryo 3D printing, although possessing the same uniformly-distributed macroporous structure, were observed, under higher magnification, to have agglomerated nHA particles on the surface as well as irregular pores (Figure S6), which could be attributed to the aggregation of nHA in the printing inks. In addition, a more continuous coating structure was observed on the PT/CHA@TA and PT/CHA@TA-Mg groups of these scaffolds, and a fuller surface deposition morphology was observed in the PT/CHA@TA-Mg scaffold group, which was attributed to the metal-polyphenol network formed by the self-polymerization in TA-Mg [35], whereas the TA coating alone presented a looser structure. The successful metal-polyphenol anchoring was confirmed by a uniform distribution of C and O signals on the surface of the TA-Mg group observed through EDS and the detection of Mg distribution signals. The stable coating structure is primarily attributed to the adhesive aggregation of TA-Mg. Furthermore, polymer scaffolds typically face difficulties in modification due to their hydrophobic surfaces and a lack of functional groups.

The surface functional group structure of the composite PT/CHA@TA-Mg scaffold was analyzed using FTIR spectroscopy (Figure 3c). Meanwhile, the C=O and -C-C-O stretching vibrational peaks belonging to LLA and TMC were observed near 1740 cm^{-1} and 1187 cm^{-1}, whereas the O-C-O vibrational peak belonging to TMC was observed near 1260 cm^{-1}. The characteristic peaks at 560 cm^{-1} and 600 cm^{-1} were also the Ca-O and P-O bending vibrational peaks of nHA respectively, confirming the presence of CHA in the scaffold. In addition, the presence of numerous phenolic hydroxyl groups in the TA molecules resulted in an -OH stretching vibration peak near 3413 cm^{-1}. Additionally, a characteristic stretching vibration peak of the conjugated double bond was observed near 1612 cm^{-1}. XPS was used to further analyze the elemental distribution of the scaffold surface coating and the formation of bonding interactions. Firstly, the elemental distribution of the scaffold surface before and after coating was analyzed using the full spectrum of XPS, and the presence of Mg was also clearly observed (Figure 3d). The high-resolution spectral analysis of O 1 s revealed peaks at 533.35 eV and 530.88 eV, attributed to the ligand bonds formed between MgO and C-O, respectively, confirming the chelating interactions of TA phenolic hydroxyl groups with Mg (Figure 3e). Similarly, the appearance of a Mg^{2+} complexation peak was observed at 1304.14 eV in the Mg 1 s deconvolution spectrum (Figure 3f). These results demonstrated that the Mg ions produced metal-polyphenol coordination through the phenolic hydroxyl groups with TA.

IBDs are often associated with a more severe inflammatory acidic microenvironment, so the rate of TA release from the coatings was measured at different pH conditions (pH 5.5 and pH 7.4) (Figure 3g). At a normal pH of 7.4, the release rate of TA from PT/CHA@TA-Mg was relatively slow. In contrast, under acidic conditions, a significant increase in drug release was observed within a short period, with ∼70% of the drugs being released on Day 6. This might be attributed to the enhanced self-assembly of the metal-polyphenol network, whereas the acidic condition resulted in the protonation of polyphenols, which decreased the binding capacity of the metal ions and thus increased the drug release rate. ICP-MS results showed a rapid Mg^{2+} release within the first 6 days, followed by sustained release for the next 12 days (Figure S8), enabling early regulation of the infectious microenvironment and prolonged local drug concentration. After 10 compression cycles, Mg^{2+} release remained unchanged compared with uncompressed scaffolds, confirming the coating's stability (Figure S7). In addition, the scavenging efficiency of different groups of scaffolds on DPPH free radicals was tested (Figure 3h), and the CHA-coated scaffolds demonstrated a certain DPPH-scavenging effect (8.92 ± 4.58%), which might be due to the certain antioxidant effect of citric acid. While the TA-coated and TA-Mg scaffolds demonstrated more significant free radical scavenging effect (77.51 ± 5.30% and 79.52 ± 8.19%), which could be attributed to the phenolic hydroxyl groups of TA that could provide a sufficient amount of hydrogen atoms to neutralize the free radicals and undergo conjugation reactions, demonstrating stronger antioxidant effects [36].

Evaluation of physicochemical properties of three dimensional printed PT/CHA@TA-Mg

The surface microtopography of scaffolds from different groups was characterized through AFM. The PT scaffolds exhibited a smooth polymer-like surface morphology, whereas the PT/CHA scaffolds showed a significantly rougher and more uneven structure as a result of CHA incorporation. As a TA-Mg coating was constructed, the scaffolds exhibited a rougher morphology, which was mainly due to the polyphenol-metal complexes enriched on their surfaces (Figure 4a), with a roughness of 252.56 ± 32.66 μm, exceeding the roughness of the PT scaffolds (56.94 ± 19.55 μm) by a factor of >4 (Figure 4c), and such homogeneous and extensive roughness could effectively increase the stem cell surfaces. Suitable hydrophilicity could also effectively improve the spreading behavior of cells on the scaffold surfaces, the hydrophilicity of the scaffolds was assessed by the contact angle (WCA) (Figure 4b), and the PT scaffolds showed a more pronounced hydrophobic

Downloaded from academic.oup.com/burnstrauma/article/doi/10.1093/burnst/tkaf072/8317955 by guest on 12 October 2026

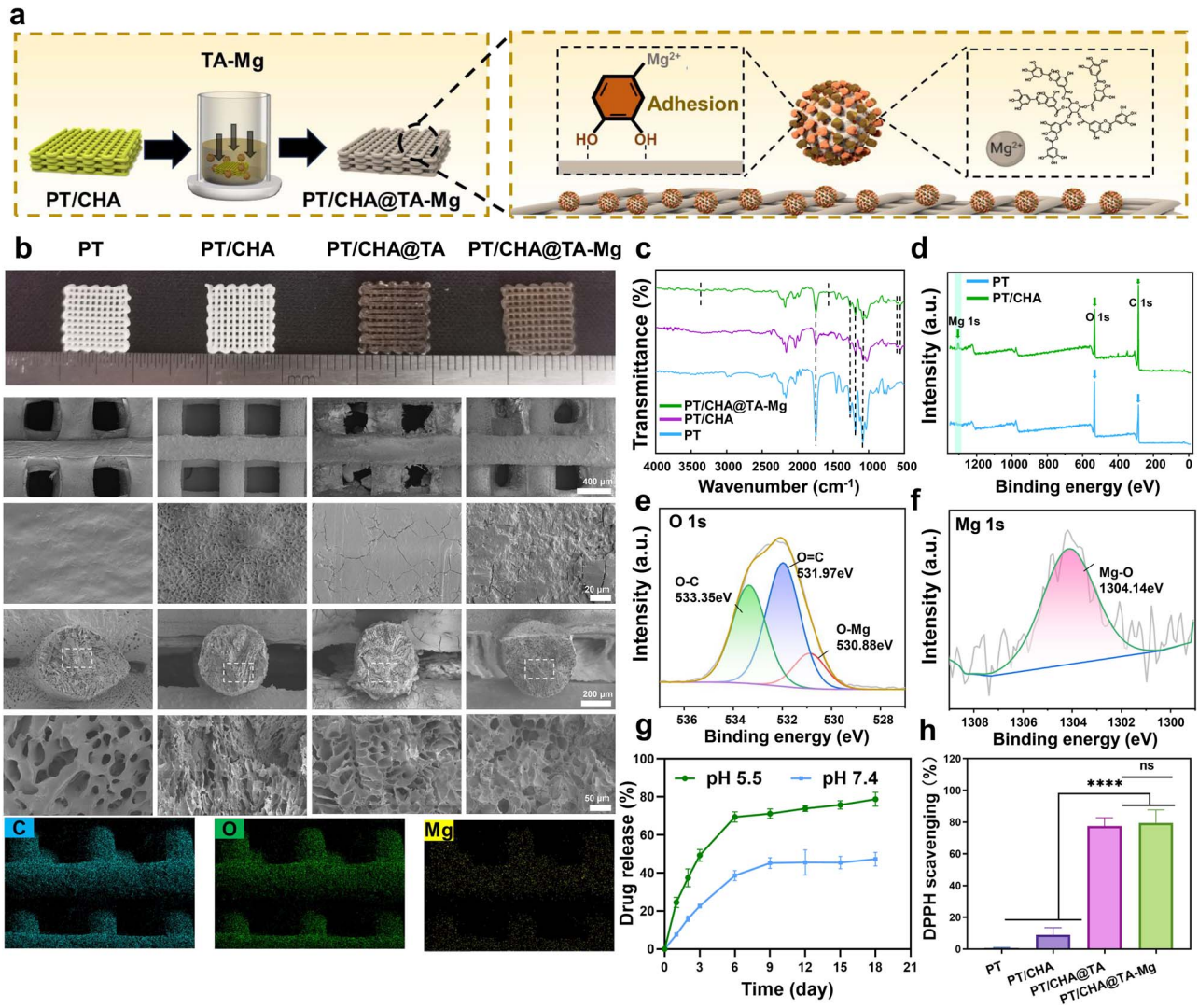


Figure 3 Construction and characterization of 3D printed metal-polyphenol coated scaffolds. (**a**) Schematic diagram of low-temperature 3D printed PT/CHA scaffolds loaded with TA-Mg coating. (**b**) Physical drawing of PT/CHA@TA-Mg scaffolds as well as SEM images of surface and cross-section morphology. (**c**) FTIR images of PT/CHA@TA-Mg scaffolds. (**d**) XPS measurement spectra of PT/CHA@TA-Mg scaffolds. (**e**) O 1s high-resolution spectra of scaffolds. (**f**) Mg 1s high-resolution spectra of scaffolds. (**g**) Drug release rates under different pH conditions. (**h**) DPPH scavenging efficiency of the scaffolds. Data are expressed as mean ± SD. $^{*}P < 0.05$, $^{**}P < 0.01$, $^{***}P < 0.001$, $^{****}P < 0.0001$, $n = 3$. *OH* hydroxyl bond, *CHA* citric acid-modified hydroxyapatite,*PT* poly(L-lactic acid)-trimethylene carbonate

structure due to the ester group (-COO-) structure of the PLA-based molecules and the tri-methylene (-C(CH_3)$_3$) clusters in the TMC structure, with a contact angle of greater than 90° (108.67 ± 1.67°) [37]. The hydrophilic nature of hydroxyapatite effectively improved the hydrophilicity of the scaffolds with the introduction of CHA. In addition, the deposition of TA and TA-Mg complexes on the scaffold surfaces further improved the hydrophilicity of the scaffolds (59.77 ± 3.61° and 47.58 ± 2.69° respectively), which was attributed to the incorporation of magnesium ions to form a metal-polyphenol structure on the denser TA coatings, generating stronger hydrophilic groups and changing the coating micromorphology, thereby reducing their contact angle with water molecules (Figure 4d) [38]. The water absorption rate of the scaffolds was also measured to observe the same trend as that of the contact angle (Figure S9). PT/CHA@TA-Mg had a water absorption rate of 45.86 ± 4.92% within 12 h, which was much higher than that of the PT scaffold (18.04 ± 1.57%).

A good compressive resistance and deformability are essential requirements for artificial bone scaffolds [39]. First of all, we conducted DSC tests on PT and PT/CHA (Figure 4e). Although the addition of CHA slightly increased the Tg of the materials, the Tg was still at ∼37°C (37.2°C and 38.6°C), indicating that the materials could deform at body temperature. Further, we prepared scaffolds containing 20% (wt%) nHA and 20% (wt%) CHA (PT/HA and PT/CHA), and conducted compressive performance tests on them at 37°C and 25°C (Figure 4f). The results showed that at 25°C, the scaffolds with HA and CHA significantly improved the mechanical properties of the scaffolds, with compressive modulus of 23.25 ± 3.59 MPa and 42.50 ± 3.38 MPa, respectively. Compared with the PT/HA scaffold, the modulus of the PT/CHA scaffold increased significantly, which might be attributed to the more uniform dispersion of CHA particles in the inks, thus increasing the average stress distribution of the scaffold when subjected to forces. Additionally, although the compressive

Downloaded from academic.oup.com/burnstrauma/article/doi/10.1093/burnst/tkaf072/8317955 by guest on 12 October 2026

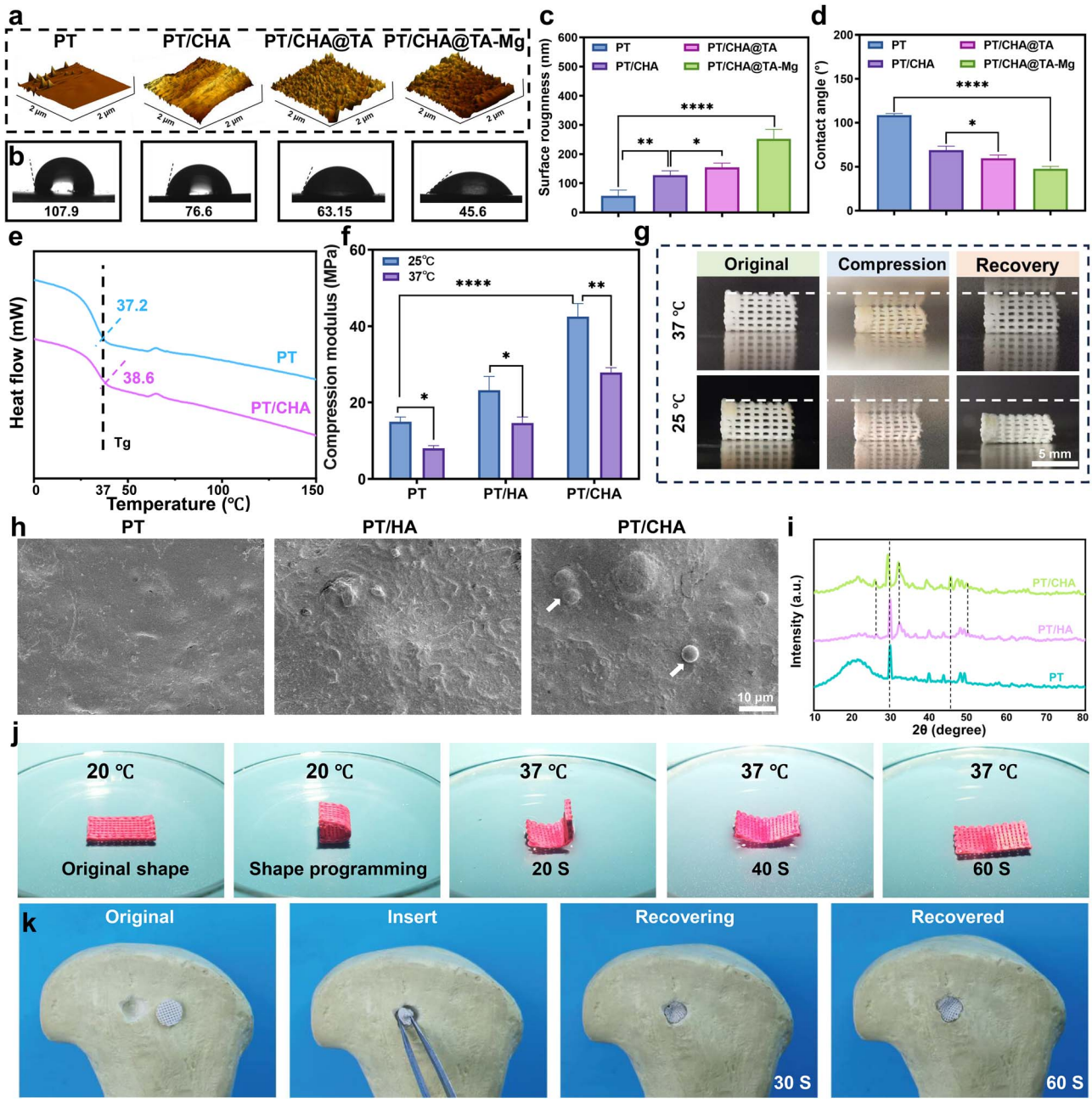


Figure 4 Physical and chemical properties evaluation of the PT/CHA@TA-Mg scaffold. (**a**) SPM image of the surface of the PT/CHA@TA-Mg scaffold. (**b**) Water contact angle image of the scaffold. (**c**) Statistics of the surface roughness of the scaffold. (**d**) Statistical analysis of the contact angle of the scaffold. (**e**) DSC tests for PT and PT/CHA. (**f**) The compressive modulus of scaffolds at 25°C and 37°C. (**g**) Shape recovery function of the scaffold after compression testing at 25°C and 37°C. (**h** and **i**) hydroxyapatite crystal formation image and XRD image of the scaffold surface after 72 h of *in vitro* mineralization (the white arrow indicates the hydroxyapatite crystal). (**j**) Shape memory function test of the scaffold. (**k**) Shape memory recovery images of the scaffold on the simulated bone. Data are expressed as mean ± SD. $^{*}P < 0.05$, $^{**}P < 0.01$, $^{***}P < 0.001$, $^{****}P < 0.0001$, $n = 3$. *CHA* citric acid-modified hydroxyapatite, *PT* poly(L-lactic acid)-trimethylene carbonate, *HA* hydroxyapatite

modulus of the scaffolds at 37°C was lower than that at 25°C, they still had a relatively obvious compressive performance advantage compared to other shape memory polymer scaffolds [40, 41]. Moreover, the shape recovery performance of the scaffolds was observed at 37°C and 25°C. When the compression temperature was 25°C, the scaffolds were compressed and fixed in a temporary shape. When the compression temperature was 37°C, due to the rearrangement of the polymer molecular chains inside the scaffolds, they exhibited good thermally-induced shape recovery performance and returned to their original shape (Figure 4g).

Using an SBF solution to simulate the mineralization behavior of the scaffolds *in vitro*, the PT scaffold without added inorganic salts was difficult to form hydroxyapatite crystals on the surface. In contrast, hydroxyapatite crystals were observed at varying degrees in the scaffolds containing nHA and CHA, and the more intact hydroxyapatite crystals on the PT/CHA scaffold surface were probably generated because the abundant carboxyl

Downloaded from academic.oup.com/burnstrauma/article/doi/10.1093/burnst/tkaf072/8317955 by guest on 12 October 2026

groups (-COOH) on the citric acid surface were able to interact with the calcium ions (Ca^{2+}) and phosphates (PO_4^{3-}), thereby enhancing the efficiency of calcium ion precipitation and thus promoting the promotion of hydroxyapatite crystallization and mineralization (Figure 4h). Further, the diffraction peaks of PT, PT/HA, and PT/CHA at the same mineralization time were evaluated by XRD (Figure 4i). Among them, the diffraction peak near 29.6° was attributed to the PLLA crystallization in the scaffolds. Compared with the PT scaffold, new hydroxyapatite diffraction peaks (25.8° and 31.7°) appeared in the mineralized PT/HA and PT/CHA scaffolds, which proved the formation of mineralized crystallization on the scaffold surfaces. In addition, the sharper diffraction peak of PT/CHA confirmed that CHA had a better ability to promote scaffold mineralization than HA under the same treatment conditions. To evaluate scaffold degradability, enzymatic degradation was performed to mimic the *in vivo* environment. Over 8 weeks, the mass loss of PT scaffolds was $11.16 \pm 1.29\%$, whereas PT/CHA scaffolds reached $20.91 \pm 1.57\%$ (Figure S10a), indicating that the incorporation of CHA effectively accelerated degradation, potentially aligning with the bone regeneration timeline. SEM images revealed that both PT and PT/CHA scaffolds exhibited slight surface shrinkage while maintaining their porous structures (Figure S11), likely due to the erosive degradation of TMC preventing brittle fracture of PLA. The pH of the degradation medium remained near neutral (Figure S10b), suggesting that TMC's neutral degradation products mitigated the acidic environment caused by PLA-derived lactic acid, supporting the scaffolds' long-term implantation.

To further validate the shape memory performance of the scaffolds *in vitro*, firstly, they were given a curved temporary shape at a temperature higher than the glass transition temperature, then they were quickly fixed to a temporary shape at a simulated surgical ambient temperature of 20°C, after which they were placed in the ambient temperature of 37°C, and it was observed that the scaffolds were restored to their original shape within 60s (Figure 4j and k). The shape memory recovery function of the scaffolds was verified by simulating the implantation environment at human body temperature, which can well circumvent the problem that artificial bone repair scaffolds cannot adapt to irregular bone defect boundaries, thus increasing the efficiency of osseointegration. In addition, the high mechanical strength of scaffolds can support the defects and rapidly induce calcium and phosphorus ion deposition in the body to promote mineralization while providing conditions for the development of osteoblasts.

Biocompatibility and osteogenic properties of scaffolds *in vitro*

The proliferation ability and viability of BMSCs were evaluated through live staining after the co-culture of scaffolds with BMSCS. After 1,3 days of co-incubation, there was no significant difference in the proliferation rate of BMSC cells at the bottom of the scaffold pore plates of PT, PT/CHA, PT/CHA@TA and PT/CHA@TA-Mg, and the cell density on Day 3 was significantly higher than that on day 1 (Figure 5a). Furthermore, we directly observed the migration of BMSCs on the surface of the scaffolds (Figure 5b). Owing to the excellent hydrophilicity of TA and its adhesive properties resembling those of "mussels", BMSCs grew extensively on the surfaces of both PT/CHA@TA and PT/CHA@TA-Mg scaffold groups. Further fluorescence intensity measurements (Figure 5f) demonstrated that the cell coverage area of the TA-Mg-coated scaffold ($12.53 \pm 0.95\%$) was significantly larger than that of the PT scaffold ($3.8 \pm 1.52\%$). Cytoskeleton staining also confirmed that both scaffolds facilitated cell spreading (Figure 5c).

The BMCSs on the PT/CHA, PT/CHA@TA, and PT/CHA@TA-Mg scaffolds were observed through SEM, which presented a more spread morphology and extended more pseudopodia (Figure 5d), confirming that the scaffolds were conducive to cell proliferation and adhesion. In addition, the CCK-8 assay results (Figure 5e) demonstrated that the OD values of all 4 groups progressively increased within co-culture durations of 1, 3, and 5 days. This finding further corroborated the scaffolds' excellent cell affinity. Subsequently, a hemolysis test was performed to evaluate the blood compatibility of the scaffolds (Figure 5g). The results revealed that, apart from the H_2O-added group that exhibited significant hemolysis, no hemolysis was observed in the PBS, PT/CHA, or PT/CHA@TA-Mg groups. Consequently, the PT/CHA@TA-Mg scaffold not only exhibited superior biocompatibility but also effectively supported cell proliferation, making it a promising candidate for subsequent bone tissue regeneration applications.

The osteogenic differentiation-promoting capability of the scaffolds was assessed using both *in vitro* qualitative and quantitative approaches. As depicted in Figure 5h, the PT/CHA@TA-Mg scaffold group demonstrated the most intense ALP staining, followed by the PT/CHA and PT/CHA@TA groups. Furthermore, a quantitative analysis of ALP activity revealed that the PT/CHA@TA-Mg group exhibited significantly higher ALP activity compared to the other groups on both Day 7 and Day 14 (Figure 5i). Furthermore, the osteogenic differentiation of BMSCs in different groups was assessed using ARS (Figure 5j and k). The PT/CHA@TA-Mg scaffold group exhibited the highest calcium nodule formation, suggesting that the sustained release of Ca^{2+} from CHA on the scaffold surfaces could induce stem cell osteogenic differentiation.

The antibacterial and anti-inflammatory activity of the scaffolds

IBDs are frequently associated with the persistent invasion of pathogenic bacteria, which disrupts the local microenvironment and delays bone tissue healing [42]. Consequently, early graft implantation that directly acts on surrounding bacteria can facilitate the rapid restoration of the bone immune microenvironment. Bacterial live-dead staining results revealed that both the control group and the PT group exhibited strong green fluorescence signals (live bacteria), whereas the PT/CHA@TA-Mg group displayed prominent red dead bacteria fluorescence signals (dead bacteria). These findings indicated that the PT/CHA@TA-Mg scaffold effectively suppressed bacterial proliferation (Figure 6a and b). The agar plate counting method was employed to further evaluate the impact of each scaffold group on the proliferation of *S. aureus* and *E. coli*. Notably, the PT/CHA@TA-Mg scaffold demonstrated the most pronounced inhibitory effect against *S. aureus*. The antibacterial activity of the other groups followed this order: Control $\approx$ PT $\approx$ PT/CHA $<$ PT/CHA@TA $<$ PT/CHA@TA-Mg (Figure 6c). In contrast, the inhibitory effect of the PT/CHA/TA and PT/CHA@TA-Mg scaffolds on *E. coli* was significantly weaker than that on *S. aureus* (Figure S12). A statistical analysis of colony

Downloaded from academic.oup.com/burnstrauma/article/doi/10.1093/burnst/tkaf072/8317955 by guest on 12 October 2026

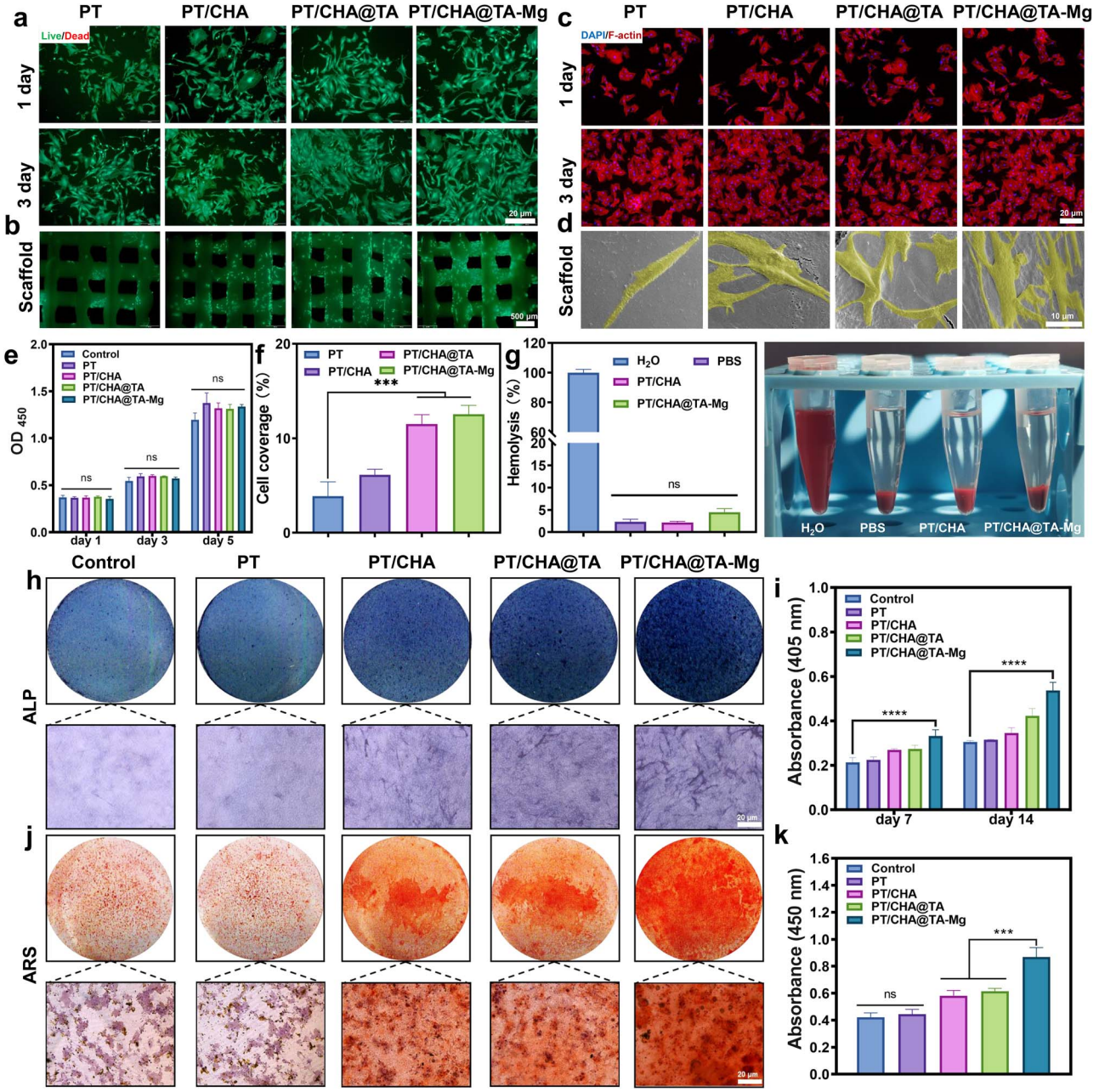


Figure 5 Biocompatibility and osteogenic differentiation performance of PT/CHA@TA-Mg scaffolds. (**a**) Live/dead fluorescence images of BMSCs co-cultured with scaffolds for 1 day and 3 days. (**b**) Proliferation and adhesion of BMSCs on the scaffold surface after co-culture for 3 days. (**c**) Fluorescence images of cytoskeleton staining of BMSCs after co-culture for 1 day and 3 days. (**d**) SEM images of BMSC on scaffolds after co-culture. (**e**) Proliferation of cells co-cultured with scaffolds for 1 day, 3 days and 5 days as determined by CCK-8. (**f**) Cell coverage area on the scaffold after co-culture for 3 days (**g**) Hemolysis test results. (**h** and **i**) Alkaline phosphatase staining and corresponding quantitative images of scaffold extract co-cultured with BMSCs. (**j** and **k**) ARS staining and corresponding quantitative images. Data are expressed as mean ± SD. $^{*}P < 0.05$, $^{**}P < 0.01$, $^{***}P < 0.001$, $^{****}P < 0.0001$, $n = 3$. *CHA* citric acid-modified hydroxyapatite, *PT* poly(L-lactic acid)-trimethylene carbonate

counts revealed that the inhibition rate of the PT/CHA@TA-Mg scaffold against *S. aureus* exceeded 90%, whereas its inhibitory effect on *E. coli* was ~60% (Figure 6d and e). Based on these findings, it can be concluded that the metal-polyphenol network coatings exhibit a more potent inactivation effect on Gram-positive bacteria. Further observation of morphological changes in the bacteria directly exposed to the TA-Mg coating was performed using SEM. Bacteria in the PT and PT/CHA groups exhibited relatively intact and smooth shapes. In contrast, *S. aureus* on the TA and TA-Mg coatings displayed obvious surface depressions and shrinkage. This phenomenon might be attributed to the release of phenolic hydroxyl groups from the coatings, which induced oxidative stress in the bacteria, leading to bacterial membrane disruption and subsequent cell death (Figure 6f and g) [43].

In addition to severe pathogen invasion, early-stage IBDs can also disrupt the immune microenvironment surrounding the defects. Macrophages, as key mediators of immune responses,

Downloaded from academic.oup.com/burnstrauma/article/doi/10.1093/burnst/tkaf072/8317955 by guest on 12 October 2026

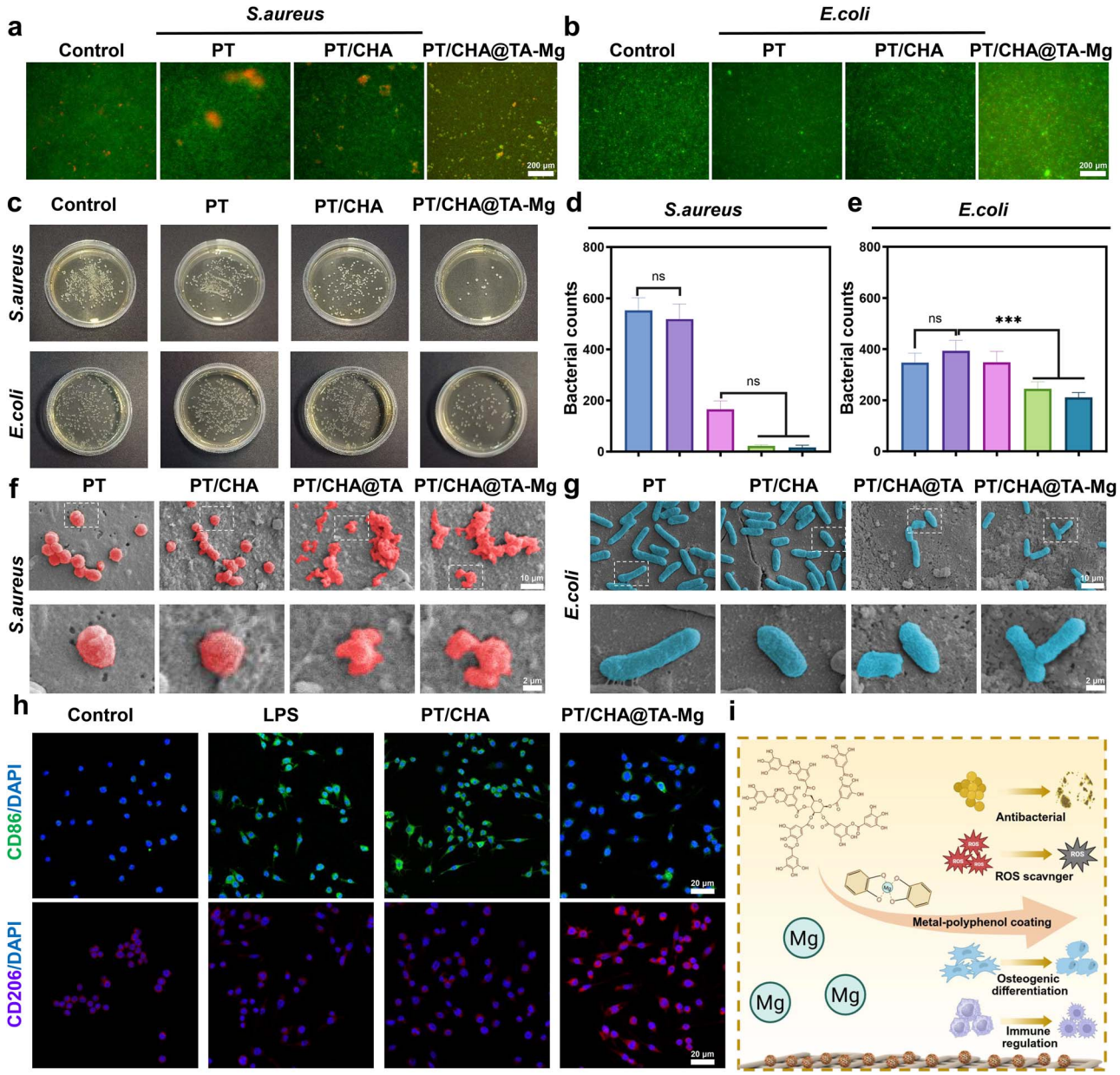


Figure 6 *In vitro* antibacterial performance and immunomodulatory capacity of PT/CHA@TA-Mg scaffolds. (**a**) Live/dead staining images of *S. aureus* co-cultured with scaffolds. (**b**) Live/dead staining images of *E. coli* co-cultured with scaffolds. (**c**) Representative images of bacterial colonies grown on agar plates after 24 h co-culture of scaffolds with bacteria in different groups. (**d**) Inhibition efficiency of *S. aureus* by scaffolds in different groups after co-culture. (**e**) Inhibition efficiency of *E. coli* by scaffolds in different groups after co-culture. (**f**) SEM images of *S. aureus* morphology after treatment with scaffolds. (**g**) SEM images of *E. coli* morphology after treatment with scaffolds. (**h**) Representative images of immunofluorescence of CD86 and CD206 in macrophages after treatment with different groups(blue: nucleus, red: CD206, green: CD86). (**i**) Schematic diagram of PT/CHA@TA-Mg scaffolds regulating the infection microenvironment. Data are expressed as mean ± SD. $^{*}P < 0.05$, $^{**}P < 0.01$, $^{***}P < 0.001$, $^{****}P < 0.0001$, $n = 3$. *LPS* lipopolysaccharide, *S. aureus Staphylococcus aureus*, *E. coli Escherichia coli*, *Mg* magnesium, *ROS* reactive oxygen species, *CHA* citric acid-modified hydroxyapatite, *PT* poly(L-lactic acid)-trimethylene carbonate

are initially stimulated into an M1 phenotype during an acute inflammatory phase and subsequently polarize toward the M2 phenotype during tissue repair. However, persistent inflammation induced by bacterial infections often impairs the balance of M1-to-M2 polarization, leading to delayed bone defect healing. Therefore, modulating the immune function of the local microenvironment represents an effective strategy for promoting bone regeneration. First of all, LPS was employed to simulate the inflammatory microenvironment of macrophages; meanwhile, the expression levels of M1 macrophage marker (CD86) and M2 macrophage marker (CD206) were evaluated via an immunofluorescence analysis. A comparison between the control group and the LPS-treated group revealed a significant upregulation in the fluorescence intensity of CD86 (green), confirming the successful induction of inflammatory activation in macrophages (Figure 6h). In contrast, samples treated with the PT/CHA@TA-Mg scaffold exhibited a marked reduction in CD86 fluorescence intensity and a notable increase in CD206 fluorescence intensity(red). A

Downloaded from academic.oup.com/burnstrauma/article/doi/10.1093/burnst/tkaf072/8317955 by guest on 12 October 2026

quantitative fluorescence intensity analysis further corroborated that PT/CHA@TA-Mg effectively promoted the upregulation of M2 phenotype markers while suppressing the expression of M1 phenotype markers (Figures S13 and S14). Flow cytometry analysis revealed that treatment with PT/CHA@TA-Mg significantly increased the proportion of macrophages polarized toward the M2 phenotype under inflammatory stimulation (Figure S15). RT-qPCR further confirmed the expression of M1 markers (iNOS and TNF-α) and M2 markers (Arg-1 and IL-10), showing that PT/CHA@TA-Mg markedly downregulated M1 markers while upregulating M2 markers, indicating promotion of anti-inflammatory macrophage polarization (Figure S16). Additionally, intracellular ROS levels were assessed by flow cytometry, and LPS-induced inflammatory macrophages exhibited elevated ROS production (Figure S17). PT/CHA@TA-Mg treatment significantly reduced intracellular ROS, suggesting that the coating promotes macrophage polarization by mitigating oxidative stress. Overall, the metal-polyphenol network of the TA-Mg coating worked synergistically to provide a favorable immune microenvironment for the PT/CHA scaffold to exert its bone regeneration capabilities. This was achieved by eliminating free radicals, regulating macrophage polarization toward the M2 phenotype, and effectively killing pathogenic bacteria, thereby enabling the spatiotemporal regulation of IBD treatment (Figure 6i).

The *in vivo* antibacterial effect of the scaffolds

An IBD model was established in SD rats, and the *in vivo* anti-infection efficacy of the scaffolds was evaluated via gross observation and histological analysis (Figure 7a). Figure 7b illustrates the macroscopic morphology of a femoral condyle defect 14 days after scaffold implantation. The bone defect was exposed by incising the purulent tissues, revealing a substantial amount of inflammatory fibrous hyperplastic tissues at the center of the defect. Both the PT group and the PT/CHA group exhibited extensive hyperplastic tissues and purulent fluid exudation around the implanted scaffold, indicating the persistence of a severe infection microenvironment surrounding the bone defect. In contrast, in the PT/CHA@TA-Mg group, a coating membrane composed of connective tissues, collagen and an extracellular matrix was observed, accompanied by well-vascularized tissues without purulent fluid or secretion exudation. This suggested that inflammation in the defect area had resolved and the tissue repair process had been initiated. In addition, after co-culture in an *in vitro* LB medium, the turbidity of PT/CHA@TA-Mg was significantly lower than that of the PT group (Figure 7c), indicating a superior sterilization efficacy of the scaffold in the *in vivo* environment. The antibacterial performance of the scaffold was assessed by incubating residual bacteria surrounding the scaffold implanted in the medium. The results demonstrated that the PT/CHA@TA-Mg group exhibited the fewest *S. aureus* colonies, confirming its outstanding antibacterial capability (Figure 7d). Serum was collected simultaneously for the detection of inflammatory factors (Figure 7e and 7f). The results demonstrated that PT/CHA@TA and PT/CHA@TA-Mg groups exhibited a more pronounced downregulation of TNF-α and IL-10 levels compared to the other groups, whereas the remaining groups still exhibited relatively high levels of inflammatory factors in the body. The early post-implantation inflammatory responses were evaluated using H&E staining and Gram staining. A substantial infiltration of inflammatory cells and bacteria was observed around the defects in both the PT and PT/CHA groups, indicating a pronounced inflammatory reaction in the surrounding tissues (Figures 7g and h). In contrast, PT/CHA@TA-Mg showed reduced neutrophil aggregation and a more pronounced antibacterial effect.

The bone repair effect of the scaffold *in vivo*

The formation of new bones in the defect area was precisely evaluated using micro-CT, as shown in Figure 8a. In both Control and PT scaffold groups, substantial bone defects were observed, which could be attributed to persistent bacterial infections and the absence of osteogenic induction factors, leading to delayed bone healing [44]. In contrast, the PT/CHA@TA-Mg group exhibited superior cancellous bone healing and the formation of a new bone bridge. This was likely due to the effective modulation of an early infection microenvironment through the release of TA-Mg, promoting enhanced new bone ingrowth. A further quantitative analysis was performed to evaluate the rate of new bone tissue ingrowth and the status of trabecular bones (Figure 8b–e), including BV/TV, Tb.N, Tb.Th, and Tb.Sp. Notably, the significantly increased Tb.Th and decreased Tb.Sp in the PT/CHA@TA-Mg scaffold group indicated the formation of more mature and denser trabecular bones. The formation of bone tissues surrounding the scaffolds was assessed via histological staining. H&E staining revealed that in both the PT/CHA@TA-Mg and PT/CHA scaffold groups, new bone ingrowth was observed across a relatively extensive area within the through-network structure (Figure 8f). In contrast, in the PT scaffold group, despite the presence of relatively well-defined pore structures, only fibrous woven bone networks were formed within the through-structure, indicating a slower osteogenesis process. Additionally, Masson staining demonstrated more prominent deep blue bone collagen deposition in the PT/CHA@TA-Mg group (Figure 8g), with a similar trend confirmed by a statistical evaluation of the collagen fiber distribution (Figure S18). Furthermore, immunohistochemistry was employed to validate the osteogenesis process within the tissues. Osteocalcin (OCN) [45], as a mid-term marker of osteoblast maturation, exhibited strong positive signals in both the PT/CHA@TA-Mg and PT/CHA scaffold groups (Figure 8h). A quantitative analysis of positive cell areas (Figure S19) further corroborated the promoting effect of TA-Mg on mid-to-late stage osteogenesis through the modulation of the immune microenvironment.

Discussion

The treatment of IBDs presents a significant challenge, particularly after extensive debridement, as it involves the integration of bone implant materials with the host bones' spatial structure. Furthermore, persistent pathogen invasion leads to continuous disruption of the local immune microenvironment, exacerbating the complexity of regenerative repair [46]. In recent years, shape-memory scaffolds have shown promising potential in bone tissue engineering due to their ability to dynamically adapt to

Downloaded from academic.oup.com/burnstrauma/article/doi/10.1093/burnst/tkaf072/8317955 by guest on 12 October 2026

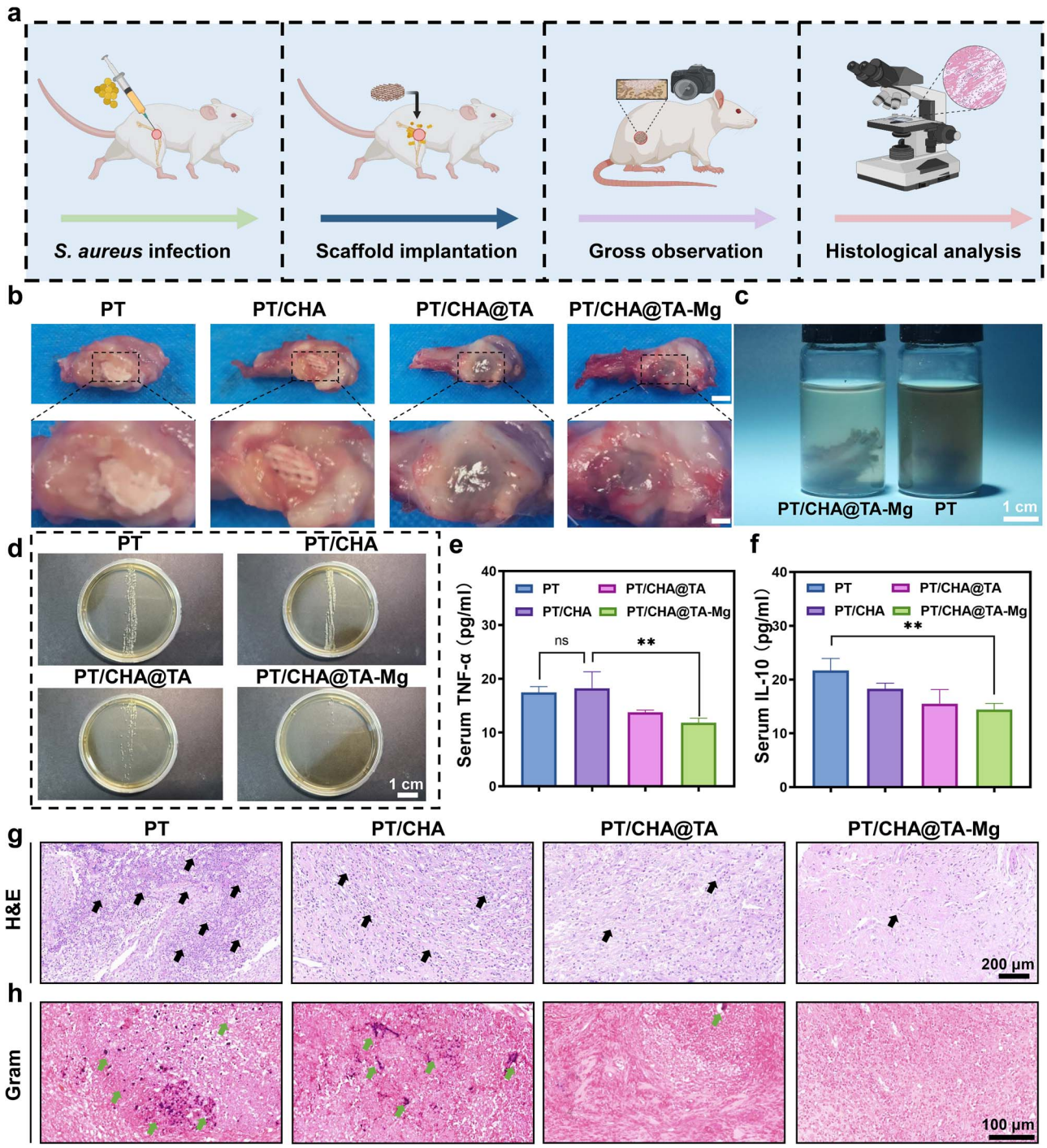


Figure 7 *In vivo* antibacterial performance of PT/CHA@TA-Mg scaffolds. (**a**) Schematic diagram of the animal experiment process for infectious bone defects. (**b**) Photographs of the femur appearance 14 days after scaffold implantation for infectious bone defects. (**c**) Photographs of the turbidity of LB culture medium after implantation of PT/CHA@TA-Mg scaffolds and PT scaffolds, respectively. (**d**) Colony growth in infected tissues after scaffold implantation. (**e**) ELISA of TNF-α in serum. (**f**) ELISA of IL-10 in serum. (**g**) H&E staining images of the surrounding tissues of the implanted scaffolds. (**h**) Gram staining images of the surrounding tissues of the implanted scaffolds. Data are expressed as mean ± SD. $^{*}P < 0.05$, $^{**}P < 0.01$, $^{***}P < 0.001$, $^{****}P < 0.0001$, $n = 3$. *CHA* citric acid-modified hydroxyapatite, *PT* poly(L-lactic acid)-trimethylene carbonate, *TNF-α* tumor necrosis factor-alpha, *IL-10* interleukin-10, *H&E* hematoxylin and eosin

irregular defect boundaries. However, existing studies have been primarily focused on enhancing the osteoinductive properties and fabrication processes of these scaffolds, with insufficient attention given to their multifunctional requirements in the complex environment of IBDs [47]. In fact, the effective repair of such defects requires scaffolds that not only maintain osteogenic activity but also enable a rapid modulation of the infection microenvironment in early stages, thereby achieving precise disease control in a spatiotemporal manner. Therefore, this study proposes a strategy for the treatment of IBDs based on spatial

Downloaded from academic.oup.com/burnstrauma/article/doi/10.1093/burnst/tkaf072/8317955 by guest on 12 October 2026

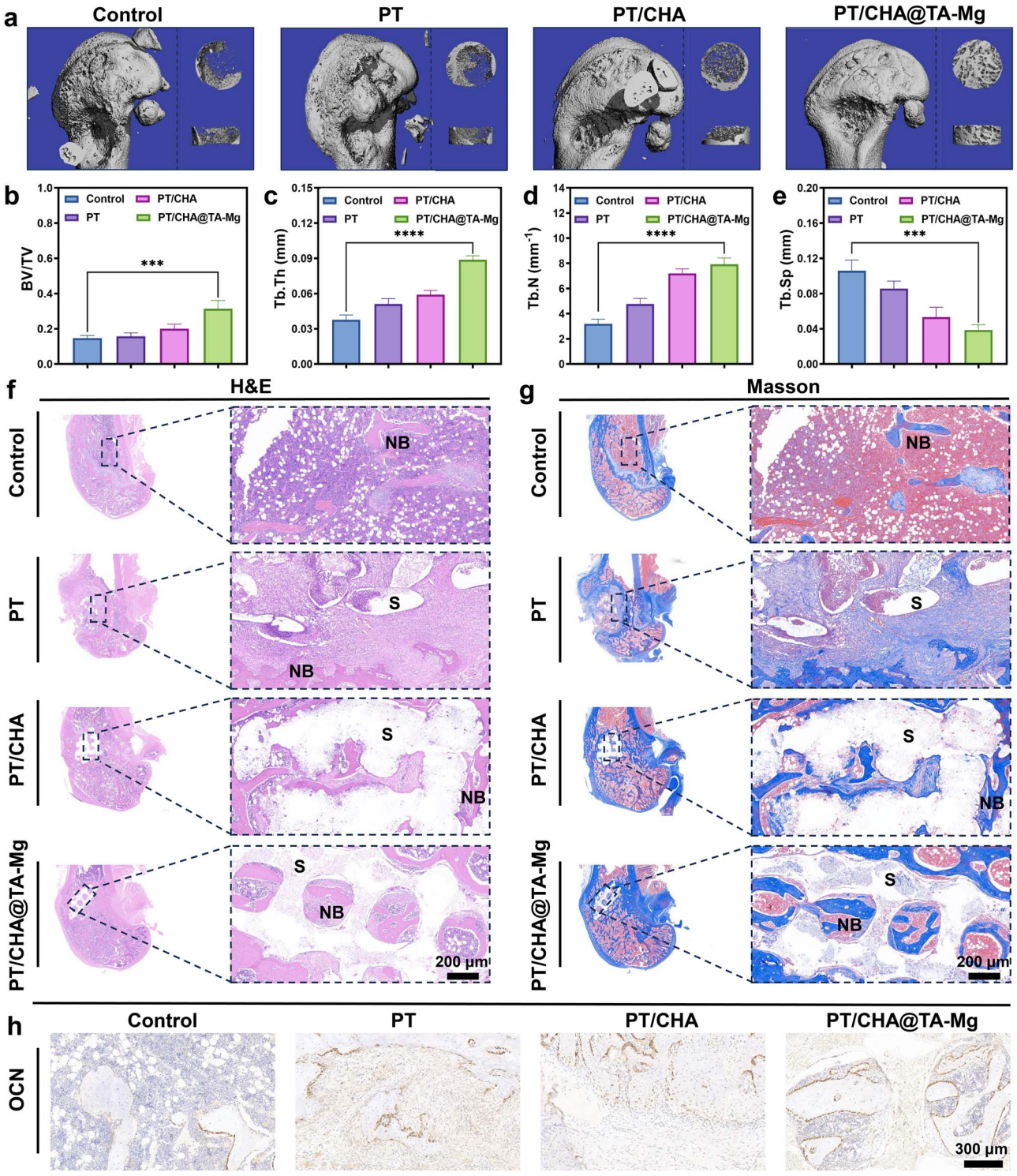


Figure 8 *In vivo* osteogenic performance of PT/CHA@TA-Mg scaffolds. (**a**) Gross view of the femur and local defect micro-CT 3D reconstruction image after 8 weeks of treatment. (**b**–**e**) quantitative analysis of BV/TV, Tb.N, Tb.Th, and Tb.Sp. (**f**) H&E staining (NB: new bone, S: scaffold) (**g**) Masson staining (NB: new bone, S: scaffold). (**h**) Immunohistochemical staining of OCN in bone tissue. Data are expressed as mean ± SD. $^{*}P < 0.05$, $^{**}P < 0.01$, $^{***}P < 0.001$, $^{****}P < 0.0001$, $n = 3$. *CHA* citric acid-modified hydroxyapatite, *PT* poly(L-lactic acid)-trimethylene carbonate

structure precision matching and the spatiotemporal sequential regulation of therapeutic effects. By combining shape-memory-based material PT with CHA and constructing a biomimetic trabecular bone multi-level porous structure scaffold via the low-temperature printing technology, we developed a scaffold with a metal-polyphenol network TA-Mg coating on the surface. This system can trigger shape-memory functionality at 37°C to fill the irregular defect boundaries after infection clearance, release TA-Mg in response to the microacidic environment in early stages to achieve the antibacterial-immunomodulatory synergistic effect, and continuously promote osteogenesis with CHA in later stages to facilitate bone regeneration.

Downloaded from academic.oup.com/burnstrauma/article/doi/10.1093/burnst/tkaf072/8317955 by guest on 12 October 2026

In traditional studies, hydrogels with good fluidity are commonly used for in situ drug-loaded treatment of IBDs. However, the rapid degradation behavior and low mechanical strength of hydrogels make it difficult to meet the spatial structural requirements of bone tissues [48]. Shape-memory scaffolds, on the other hand, can be used in combination with 3D printing technology to achieve the biomimetic filling of trabecular bone structures through stimulus-responsive mechanisms, though they still face challenges related to insufficient mechanical strength [40, 41]. In this study, a porous-structure scaffold was constructed using low-temperature printing, combining PT with citric CHA, addressing the issue of thermal degradation of polymers during high-temperature printing. *In vitro* physicochemical characterization demonstrated that the incorporation of CHA significantly enhanced the hydrophilicity and surface roughness of the scaffold (Figure 4a and b), alleviating the inherent hydrophobicity and smooth morphology of the polymer, thereby providing an excellent platform for cell proliferation and adhesion. Additionally, the citric-acid-modified CHA effectively increased the inorganic salt content in polymer inks, leading to an increase in the scaffold's compressive modulus to 42.50 ± 3.38 MPa (Figure 4f), solving the issue of insufficient mechanical strength of existing shape-memory scaffolds. Furthermore, compared to scaffolds loaded with nHA, the CHA-modified scaffold significantly improved the mineralization capability (Figure 4h and i). Moreover, unlike existing shape-memory scaffolds, which require external activation through stimuli such as infrared or acoustic-electric stimulation, the scaffold in this study exhibited excellent shape recovery performance at 37°C, which significantly simplified surgical procedures and ensured stable therapeutic outcomes (Figure 4J and K).

The pathological process of IBDs involves complex interactions between microorganisms and the host's bones, as well as the dynamic evolution of the bone repair microenvironment [49]. Traditional single-regulation strategies (such as promoting osteogenesis or antimicrobial activity alone) are insufficient for functional regeneration. As a result, current research is more focused on guiding the formation of the bone regeneration microenvironment in both time and space through scaffolds. Based on the effectiveness of PT/CHA scaffolds in promoting osteogenesis, we developed a TA-Mg coating with a metal-polyphenol network structure. The "mussel" effect of TA allows for an efficient accumulation of the coating on the scaffold surface, improving the polymer scaffold's relatively inert surface that cannot typically load drugs efficiently [50]. *In vitro* experiments showed that the coating could rapidly release in response to the infection-induced acidic environment (Figure 3g). Antibacterial assays demonstrated that the coating effectively inhibited bacterial growth. Notably, TA-Mg exhibited stronger inhibitory effects against Gram-positive bacteria such as *S. aureus*, while its effect on Gram-negative bacteria like *E. coli* was relatively weaker. This can be attributed to the mechanism of TA, a polyphenol, which primarily exerts antibacterial activity by disrupting the cell membrane, causing leakage of cellular contents, and interfering with membrane proteins. In Gram-positive bacteria, the thick peptidoglycan layer allows direct contact with polyphenols, enabling effective action on the cell membrane and intracellular targets, thereby resulting in higher inhibition. In contrast, Gram-negative bacteria possess an outer membrane rich in LPS, which acts as a barrier limiting polyphenol penetration to the inner membrane and intracellular targets, thus reducing the antibacterial effect [51]. Magnesium ions (Mg^{2+}), key biological ions with both osteogenic and immune-modulating functions, activate osteogenic signaling pathways such as Wnt/β-catenin and MAPK [52]. Osteogenesis assays showed that PT/CHA@TA-Mg effectively promoted the osteogenic differentiation of BMSCs and mineralization (Figures 5h and j). Additionally, a fluorescent staining analysis of macrophage markers indicated that the TA-Mg coating effectively upregulated the expression of M2 macrophage markers (Figure 6h). Literature reports indicate that implanted materials typically transition from the inflammatory phase to the proliferative phase within 14 days after surgery, a process dependent on the chemokines and growth factors secreted by M2 macrophages, which promote the migration and osteogenic differentiation of BMSCs [53]. After implanting the PT/CHA@TA-Mg scaffold into the IBD area, bacterial co-culture and histological staining analyses showed that the scaffold effectively eliminated early-stage pathogens (antibacterial rate $> 90\%$), significantly reduced the number of neutrophils, and alleviated acute inflammatory responses in the defect area, consistent with reported time points in the literature (Figures 7d–h) [54]. Micro-CT results showed that after 8 weeks of implantation, the PT/CHA@TA-Mg scaffold exhibited a good bone regeneration capability (Figure 8a). OCN staining further revealed that the PT/CHA@TA-Mg scaffold group showed higher positive expression levels, further confirming its mechanism of promoting bone regeneration through the regulation of the early infection microenvironment.

In conclusion, the PT/CHA@TA-Mg scaffold effectively integrates the interface of irregular bone defects after infectious debridement. In early stages, the TA-Mg coating achieves rapid pathogen elimination and macrophage polarization, regulating the infection microenvironment. Subsequently, PT/CHA provides sufficient mechanical strength and continuously releases Ca^{2+} while synergizing with Mg^{2+} to promote bone regeneration. However, there are still some limitations in this study. The compressive modulus of the PT/CHA scaffold is 40 MPa, which, although significantly higher than traditional shape-memory materials, still falls short of the mechanical strength of cancellous bones ($>$100 MPa) [55]. These issues will be further improved in the future.

Conclusions

In this study, we addressed the complex pathological microenvironment in the early stage of IBDs and the difficulty of artificial bone scaffolds in achieving spatial structure and mechanical strength integration within defect areas. We utilized a thermosensitive shape memory polymer PT combined with citric-acid-modified nano-hydroxyapatite (CHA) to construct a biomimetic multi-level porous PT/CHA scaffold, which exhibits both self-adaptive filling capability and mechanical support. On this basis, a metal-polysaccharide network coating (TA-Mg) was fabricated on the scaffold surface, enabling an integrated cascade repair PT/CHA@TA-Mg scaffold with antibacterial, anti-inflammatory, and osteogenic-promoting functions. Specifically, the incorporation of CHA effectively enhanced the stability of inorganic phase extrusion in the low-temperature printing system while increasing the loading capacity, thereby improving the mechanical strength of the scaffold within the defect areas and accelerating its mineralization process through citric-acid-mediated regulation of endogenous as well as exogenous calcium concentrations. Meanwhile, the TA-Mg-coated scaffold could

Downloaded from academic.oup.com/burnstrauma/article/doi/10.1093/burnst/tkaf072/8317955 by guest on 12 October 2026

rapidly disintegrate in response to the acidic microenvironment associated with infections, combating the continuous invasion of pathogenic bacteria and promoting macrophage polarization from pro-inflammatory to anti-inflammatory phenotypes, thus modulating the local immune microenvironment. This sequential treatment strategy, characterized by good antibacterial activity followed by sustained osteogenic promotion, demonstrates significant potential for the treatment of IBDs. The multifunctional platform developed in this study can be extended to various models, offering new possibilities for regenerative tissue engineering applications.

Author contributions

Shuhao Yang (Methodology [lead], Writing—original draft [lead]), Qianshui Hu (Methodology [lead], Writing—original draft [equal]), Yingkun Hu (Methodology [equal], Writing—original draft [supporting]), Zhengguang Pu (Investigation [equal], Methodology [equal]), Yixuan Lan (Investigation [equal], Methodology [equal]), Haoming Wu (Formal analysis [equal], Funding acquisition [equal]), Gaohui Zhu (Formal analysis [supporting], Funding acquisition [supporting]), Zhixiang Gao (Formal analysis [equal], Funding acquisition [equal]), Jianye Yang (Formal analysis [supporting], Funding acquisition [supporting]), Shuai Tan (Conceptualization [supporting], Project administration [supporting]), Ning Hu (Conceptualization [supporting], Project administration [equal]), and Xulin Hu (Conceptualization [lead], Project administration [lead]), Leilei Qin (Conceptualization [lead], Project administration [equal])

Supplementary data

Supplementary data is available at *Burns & Trauma Journal* online.

Ethics approval

All *in vivo* ethical approvals were granted by the Animal Ethics Center of Sichuan University under the approval number YSY-DWLL-2023252.

Conflict of interest

None declared.

Funding

This work was supported by the National Natural Science Foundation of China (NSFC, # 82402822, #82402836, #82372425), Natural Science Foundation of Sichuan Province (#23NSFSC5880), Central Guidance for Local Science and Technology Development Project (#2024ZYD0155), Chongqing Graduate Innovation Project (#CYS240290). Chongqing Natural Science Foundation General Project (CSTB2024NSCQ-MSX0921).

References

1. Ou Z, Wei J, Lei J, Wu D, Tong B, Liang H. *et al.* Biodegradable Janus sonozyme with continuous reactive oxygen species regulation for treating infected critical-sized bone defects. *Nat Commun* 2024;15:10525. https://doi.org/10.1038/s41467-024-54894-8.
2. Qin L, Yang S, Zhao C, Yang J, Li F, Xu Z. *et al.* Prospects and challenges for the application of tissue engineering technologies in the treatment of bone infections. *Bone Research* 2024;12:28. https://doi.org/10.1038/s41413-024-00332-w.
3. Zheng F, Wan X, Zhang Y, Yue Y, Li Q, Zhang Z. *et al.* A multimodal defect-rich nanoreactor triggers sono-piezoelectric tandem catalysis and iron metabolism disruption for implant infections, Science. *Advances* 2025;11:eads8694. https://doi.org/10.1126/sciadv.ads8694.
4. Hu X, Chen J, Yang S, Zhang Z, Wu H, He J. *et al.* 3D printed multifunctional biomimetic bone scaffold combined with TP-Mg nanoparticles for the infectious bone defects repair. *Small* 2024;20:2403681. https://doi.org/10.1002/smll.202403681.
5. Masters EA, Ricciardi BF, Bentley KLM, Moriarty TF, Schwarz EM, Muthukrishnan G. Skeletal infections: microbial pathogenesis, immunity and clinical management. *Nat Rev Microbiol* 2022;20:385–400. https://doi.org/10.1038/s41579-022-00686-0.
6. Lee J, Byun H, Madhurakkat Perikamana SK, Lee S, Shin H. Current advances in immunomodulatory biomaterials for bone regeneration. *Adv Healthc Mater* 2019;8:e1801106. https://doi.org/10.1002/adhm.201801106.
7. Chen J, Zhou H, Fan Y, Gao G, Ying Y, Li J. 3D printing for bone repair: coupling infection therapy and defect regeneration. *Chem Eng J* 2023;471:144537. https://doi.org/10.1016/j.cej.2023.144537.
8. Su N, Villicana C, Yang F. Immunomodulatory strategies for bone regeneration: a review from the perspective of disease types. *Biomaterials* 2022;286:121604. https://doi.org/10.1016/j.biomaterials.2022.121604.
9. He Y, Zeng F, Quan H, Liu L, Dai J, Jiang H. *et al.* Strontium-loaded multifunctional gelatin methacryloyl hydrogels for type-H vascularized bone regeneration under osteoporotic conditions. *Mater Today Bio* 2025;32:101909. https://doi.org/10.1016/j.mtbio.2025.101909.
10. Yin B, Dodda JM, Wong SHD, Deen GR, Bate JS, Pachauri A. *et al.* Smart injectable hydrogels for periodontal regeneration: recent advancements in biomaterials and biofabrication strategies. *Mater Today Bio* 2025;32:101855. https://doi.org/10.1016/j.mtbio.2025.101855.
11. Feng P, Zhao R, Tang W, Yang F, Tian H, Peng S. *et al.* Structural and functional adaptive artificial bone: materials, fabrications, and properties. *Adv Funct Mater* 2023;33:2214726. https://doi.org/10.1002/adfm.202214726.
12. Zhou J, Georgas E, Su Y, Zhou J, Kröger N, Benn F. *et al.* Evolution from bioinert to bioresorbable: in vivo comparative study of additively manufactured metal bone scaffolds. *Adv Sci* 2023;10:e2302702. https://doi.org/10.1002/advs.202302702.
13. Li J, Fan M, Jiao Z, Chan YK, Cheng L, Li J. *et al.* Glucose-gated nanocoating endowing polyetheretherketone implants for enzymatic gas therapy to boost infectious diabetic osseointegration. *Nano Today* 2024;59:102541. https://doi.org/10.1016/j.nantod.2024.102541.
14. Wu H, Yang S, Li J, Ma T, Yang K, Liao T. *et al.* Current status and challenges of shape memory scaffolds in biomedical applications. *MedComm–Biomaterials and Applications* 2024;3:e95. https://doi.org/10.1002/mba2.95.

Downloaded from academic.oup.com/burnstrauma/article/doi/10.1093/burnst/tkaf072/8317955 by guest on 12 October 2026

15. Xia Y, He Y, Zhang F, Liu Y, Leng J. A review of shape memory polymers and composites: mechanisms, materials, and applications. *Adv Mater* 2021;33:2000713. https://doi.org/10.1002/adma.202000713.
16. Jiang Y, Leng J, Zhang J. A high-efficiency way to improve the shape memory property of 4D-printed polyurethane/polylactide composite by forming in situ microfibers during extrusion-based additive manufacturing. *Addit Manuf* 2021;38:101718. https://doi.org/10.1016/j.addma.2020.101718.
17. Rosli NA, Karamanlioglu M, Kargarzadeh H, Ahmad I. Comprehensive exploration of natural degradation of poly (lactic acid) blends in various degradation media: a review. *Int J Biol Macromol* 2021;187:732–41. https://doi.org/10.1016/j.ijbiomac.2021.07.196.
18. Hu X, Zhao W, Zhang Z, Xie J, He J, Cao J. *et al.* Novel 3D printed shape-memory PLLA-TMC/GA-TMC scaffolds for bone tissue engineering with the improved mechanical properties and degradability. *Chin Chem Lett* 2023;34:107451. https://doi.org/10.1016/j.cclet.2022.04.049.
19. Hu X, Cheng S, Liu S, Zhou M, Liu J, Wei J. *et al.* Fast shape memory function and personalized PLTMC/SIM/MBG composite scaffold for bone regeneration. *Materials Today Bio* 2025;32:101791. https://doi.org/10.1016/j.mtbio.2025.101791.
20. Li C, Zhang W, Nie Y, Du X, Huang C, Li L. *et al.* Time-sequential and multi-functional 3D printed MgO2/PLGA scaffold developed as a novel biodegradable and bioactive bone substitute for challenging postsurgical osteosarcoma treatment. *Adv Mater* 2024;36:e2308875. https://doi.org/10.1002/adma.202308875.
21. Wang G, Lv Z, Wang T, Hu T, Bian Y, Yang Y. *et al.* Surface functionalization of hydroxyapatite scaffolds with MgAlEu-LDH nanosheets for high-performance bone regeneration. *Adv Sci* 2023;10:e2204234. https://doi.org/10.1002/advs.202204234.
22. Qin D, Zhao Y, Cheng R, Liu Y, Guo S, Sun L. *et al.* Mussel-inspired immunomodulatory and osteoinductive dual-functional hydroxyapatite nanoplatform for promoting bone regeneration. *J Nanobiotechnology* 2024;22:320. https://doi.org/10.1186/s12951-024-02593-3.
23. Xu H, Yan S, Gerhard E, Xie D, Liu X, Zhang B. *et al.* Citric acid: a nexus between cellular mechanisms and biomaterial innovations. *Adv Mater* 2024;36:e2402871. https://doi.org/10.1002/adma.202402871.
24. Martin V, Ribeiro IA, Alves MM, Gonçalves L, Claudio RA, Grenho L. *et al.* Engineering a multifunctional 3D-printed PLA-collagen-minocycline-nanoHydroxyapatite scaffold with combined antimicrobial and osteogenic effects for bone regeneration. *Mater Sci Eng C* 2019;101:15–26. https://doi.org/10.1016/j.msec.2019.03.056.
25. Ruiz-Agudo E, Ruiz-Agudo C, Di Lorenzo F, Alvarez-Lloret P, Ibañez-Velasco A, Rodriguez-Navarro C. Citrate stabilizes hydroxylapatite precursors: implications for bone mineralization. *ACS Biomater Sci Eng* 2021;7:2346–57. https://doi.org/10.1021/acsbiomaterials.1c00196.
26. Xu N, Gao Y, Li Z, Chen Y, Liu M, Jia J. *et al.* Immunoregulatory hydrogel decorated with tannic acid/ferric ion accelerates diabetic wound healing via regulating macrophage polarization. *Chem Eng J* 2023;466:143173. https://doi.org/10.1016/j.cej.2023.143173.
27. Song R, Wang X, Johnson M, Milne C, Lesniak-Podsiadlo A, Li Y. *et al.* Enhanced strength for double network hydrogel adhesive through cohesion-adhesion balance. *Adv Funct Mater* 2024;34:2313322. https://doi.org/10.1002/adfm.202313322.
28. Luo H, Xie J, Su X, Wang P, Chen H, Kuang X. *et al.* Tannic acid-based metal-phenolic networks as a versatile platform to mediate cell therapy. *Sci China Mater* 2024;67:1–16.
29. Qiao W, Wong KH, Shen J, Wang W, Wu J, Li J. *et al.* TRPM7 kinase-mediated immunomodulation in macrophage plays a central role in magnesium ion-induced bone regeneration. *Nat Commun* 2021;12:2885. https://doi.org/10.1038/s41467-021-23005-2.
30. Hu X-L, Mi S, Lu J-L, Cao J-F, Xing L-Y, Lin Z-D. *et al.* In vitro degradation behavior of shape memory PLLA-TMC random copolymers. *Colloids Surf A Physicochem Eng Asp* 2021;615:126220. https://doi.org/10.1016/j.colsurfa.2021.126220.
31. Wu X, Xia Y, Dai H, Hong C, Zhao Y, Wei W. *et al.* Metabolic control during macrophage polarization by a citrate-functionalized scaffold for maintaining bone homeostasis. *Adv Healthc Mater* 2024;13:e2400770. https://doi.org/10.1002/adhm.202400770.
32. Dong Z, Cui H, Zhang H, Wang F, Zhan X, Mayer F. *et al.* 3D printing of inherently nanoporous polymers via polymerization-induced phase separation. *Nat Commun* 2021;12:247. https://doi.org/10.1038/s41467-020-20498-1.
33. Hu Z, Li M, Lyu Q, Chen X, Zhang X, Yu Y. *et al.* Supramolecular 3D printing enabling one-step generation of healable and recyclable structurally colored objects. *Adv Funct Mater* 2024;34:2410921. https://doi.org/10.1002/adfm.202410921.
34. Liu X, Wang Z. Chitosan-calcium carbonate scaffold with high mineral content and hierarchical structure for bone regeneration. *Smart Mater Med* 2023;4:552–61. https://doi.org/10.1016/j.smaim.2023.04.004.
35. Zhang Q-Y, Tan J, Huang K, Nie R, Feng Z-Y, Zou C-Y. *et al.* Polyphenolic-modified cellulose acetate membrane for bone regeneration through immunomodulation. *Carbohydr Polym* 2023;305:120546. https://doi.org/10.1016/j.carbpol.2023.120546.
36. Zou YP, Liang HF, Wang B, Zhang QC, Su DH, Lu SY. *et al.* Precipitation-based silk fibroin fast gelling, highly adhesive, and magnetic nanocomposite hydrogel for repair of irregular bone defects. *Adv Funct Mater* 2023;33:2302442. https://doi.org/10.1002/adfm.202302442.
37. Xie L, Wang G, Wu Y, Liao Q, Mo S, Ren X. *et al.* Programmed surface on poly (aryl-ether-ether-ketone) initiating immune mediation and fulfilling bone regeneration. *Innovation* 2021;2:100148. https://doi.org/10.1016/j.xinn.2021.100148.
38. Zhang B, Yao R, Li L, Wang Y, Luo R, Yang L. *et al.* Green tea polyphenol induced Mg(2+)-rich multilayer conversion coating: toward enhanced corrosion resistance and promoted in situ endothelialization of AZ31 for potential cardiovascular applications. *ACS Appl Mater Interfaces* 2019;11:41165–77. https://doi.org/10.1021/acsami.9b17221.
39. Yuan X, Zhu W, Yang Z, He N, Chen F, Han X. *et al.* Recent advances in 3D printing of smart scaffolds for bone tissue engineering and regeneration. *Adv Mater* 2024;36:e2403641. https://doi.org/10.1002/adma.202403641.

Downloaded from academic.oup.com/burnstrauma/article/doi/10.1093/burnst/tkaf072/8317955 by guest on 12 October 2026

40. Zhang W, Yu M, Cao Y, Zhuang Z, Zhang K, Chen D. *et al.* An anti-bacterial porous shape memory self-adaptive stiffened polymer for alveolar bone regeneration after tooth extraction. *Bioact Mater* 2023;21:450–63. https://doi.org/10.1016/j.bioactmat.2022.08.030.
41. Zhang Y, Li C, Zhang W, Deng J, Nie Y, Du X. *et al.* 3D-printed NIR-responsive shape memory polyurethane/magnesium scaffolds with tight-contact for robust bone regeneration. *Bioact Mater* 2022;16:218–31. https://doi.org/10.1016/j.bioactmat.2021.12.032.
42. Duan Y, Li Y, Wang Y, Su L, Li Q, Jiang F. *et al.* An all-in-one "multifunctional hydrogel": through antibacterial, anti-inflammatory, and angiogenic to promoting MRSA-infected bone defect repair. *Chem Eng J* 2025;503:158132. https://doi.org/10.1016/j.cej.2024.158132.
43. Ye Y, Zheng Q, Wang Z, Wang S, Lu Z, Chu Q. *et al.* Metal-phenolic nanoparticles enhance low temperature photothermal therapy for bacterial biofilm in superficial infections. *J Nanobiotechnology* 2024;22:713. https://doi.org/10.1186/s12951-024-02985-5.
44. Li Z, He D, Guo B, Wang Z, Yu H, Wang Y. *et al.* Self-promoted electroactive biomimetic mineralized scaffolds for bacteria-infected bone regeneration. *Nat Commun* 2023;14:6963. https://doi.org/10.1038/s41467-023-42598-4.
45. Yu C, Ying X, Shahbazi M-A, Yang L, Ma Z, Ye L. *et al.* A nano-conductive osteogenic hydrogel to locally promote calcium influx for electro-inspired bone defect regeneration. *Biomaterials* 2023;301:122266. https://doi.org/10.1016/j.biomaterials.2023.122266.
46. Chen Q, Ma J, Yu S, Su Y, Guo H, Jiang H. *et al.* "Small dots, multiple functions": unveiling the veil of a bioactive quercetin carbon dot and its multifaceted antibacterial and osteogenesis mechanisms for infectious bone defect repair. *Adv Funct Mater* 2025;2507840. https://doi.org/10.1002/adfm.202507840.
47. Lyu J, Chen H, Luo J, Lin S, Yang G, Zhou M. *et al.* Shape memory and hemostatic silk-laponite scaffold for alveolar bone regeneration after tooth extraction trauma. *Int J Biol Macromol* 2024;260:129454. https://doi.org/10.1016/j.ijbiomac.2024.129454.
48. Xiao L, Wang Y, Cai J, Hu J, Dou H, Zhu Y. *et al.* MXene and near-infrared carbon dots co-encapsulated hydrogel facilitates infected bone defect reconstruction. *Adv Healthc Mater* 2025;14:e2500248. https://doi.org/10.1002/adhm.202500248.
49. Xu J, Zhou F, Cao L, Wang H, Hu J, Qiu S. *et al.* ROS-balancing-engineered bio-heterojunction hydrogel accelerated the infected bone regeneration based on Sono-chemo dynamic therapy. *Bioact Mater* 2025;52:440–59. https://doi.org/10.1016/j.bioactmat.2025.05.031.
50. Xu K, Wu X, Zhang X, Xing M. Bridging wounds: tissue adhesives' essential mechanisms, synthesis and characterization, bioinspired adhesives and future perspectives. *Burns Trauma* 2022;10:tkac033. https://doi.org/10.1093/burnst/tkac033.
51. Hosseini M, Moghaddam L, Barner L, Cometta S, Hutmacher DW, Savi FM. The multifaceted role of tannic acid: from its extraction and structure to antibacterial properties and applications. *Prog Polym Sci* 2025;160:101908. https://doi.org/10.1016/j.progpolymsci.2024.101908.
52. Li S, Li Z, Yang J, Ha Y, Zhou X, He C. Inhibition of sympathetic activation by delivering calcium channel blockers from a 3D printed scaffold to promote bone defect repair. *Adv Healthc Mater* 2022;11:e2200785. https://doi.org/10.1002/adhm.202200785.
53. Jin S, Wen J, Zhang Y, Mou P, Luo Z, Cai Y. *et al.* M2 macrophage-derived exosome-functionalized topological scaffolds regulate the foreign body response and the coupling of angio/osteoclasto/osteogenesis. *Acta Biomater* 2024;177:91–106. https://doi.org/10.1016/j.actbio.2024.01.043.
54. Sun M, Xu C, Wu R, Yang Q, Ding X, Zhao N. *et al.* Surface-engineered orthopedic implant to break the antimicrobial-osteogenic paradox at biointerfaces in the "race for the surface". *Adv Mater* 2025;37:2506113. https://doi.org/10.1002/adma.202506113.
55. Qin Y, Jing Z, Zou D, Wang Y, Yang H, Chen K. *et al.* A metamaterial scaffold beyond modulus limits: enhanced osteogenesis and angiogenesis of critical bone defects. *Nat Commun* 2025;16:2180. https://doi.org/10.1038/s41467-025-57609-9.

Downloaded from academic.oup.com/burnstrauma/article/doi/10.1093/burnst/tkaf072/8317955 by guest on 12 October 2026

© The Author(s) 2025. Published by Oxford University Press. This is an Open Access article distributed under the terms of the Creative Commons Attribution-NonCommercial License (https://creativecommons.org/licenses/by-nc/4.0/), which permits non-commercial re-use, distribution, and reproduction in any medium, provided the original work is properly cited. For commercial re-use, please contact reprints@oup.com for reprints and translation rights for reprints. All other permissions can be obtained through our RightsLink service via the Permissions link on the article page on our site—for further information please contact journals.permissions@oup.com.
Burns & Trauma, 2026, 14, tkaf072
https://doi.org/10.1093/burnst/tkaf072
Research Article